Modeling of biphasic oil-water flow in horizontal pipes using CFD for the prediction of flow patterns

Santiago Hernández García

Thesis presented for the Mechanical Engineering Degree

Director

Octavio Andrés González Estrada

PhD in Mechanical and Materials Engineering

Codirector

Germán González Silva

PhD in Chemical Engineering

Universidad Industrial de Santander

Faculty of Physicomechanical Engineering

School of Mechanical Engineering

Bucaramanga

2022

Dedicatoria

A mi madre, que con su incondicional apoyo en este proceso me ha hecho sentir que tengo la capacidad de lograr todo lo que me proponga y que por medio del ejemplo me motivó a afrontar los mayores retos sin importar su dificultad.

A mi hermano, que sirvió como un espacio de calma en los momentos más requeridos, pudiendo contar con su compañía y comprensión en todo momento.

A mi familia, que estuvo siempre atenta a mi progreso como persona y como futuro profesional.

A los amigos que conocí en este proceso ya que han sido una pieza fundamental en mi evolución como persona en este transcurso de tiempo.

Agradecimientos

A la UIS, mi alma mater, por servir como el espacio del saber dónde me pude desarrollar integralmente tanto personalmente como profesionalmente.

Al profesor Octavio Andrés González Estrada por su constante acompañamiento y disposición en el transcurso del proyecto.

Al profesor Germán González Silva y a la ingeniera Natalia Prieto Jiménez por compartir conmigo su conocimiento indispensable para la culminación del trabajo de grado.

A los profesores que con su vocación y dedicación me brindaron valiosas enseñanzas a lo largo de este proceso.

Content Table

Page

Table List

Page

Figure List

Page

Appendix List

Page

Resumen

Título: Modelado del flujo bifásico agua-aceite in tubería horizontal usando CFD para la predicción de patrones de flujo[*]

Autor: Santiago Hernández García[**]

Palabras Clave: CFD, Flujo agua-aceite, Patrón de flujo, Modelo multifásico

Descripción: Se realizó un estudio CFD del flujo horizontal agua-aceite utilizando los modelos multifásicos Euleriano-Euleriano y de mezcla en conjunto con el modelo de turbulencia *k-ε* realizable. Los modelos numéricos se realizaron utilizando agua y un aceite mineral con una densidad de 880 kg/m^3 y una viscosidad de 180 cP, variando las velocidades superficiales de ambos fluidos en rangos de 0.1–1.2 m/s y 0.1–0.5 m/s respectivamente. Bajo estas condiciones, ingresando los fluidos en estado de mezcla, el patrón estratificado pudo formarse adecuadamente con los dos modelos multifásicos. Aunque el modelo Euleriano-Euleriano, junto al esquema de reconstrucción geométrica, permitió visualizar los patrones dispersos tridimensionales de manera muy similar a los resultados experimentales, el modelo de mezcla no mostró tal similitud, especialmente en las dispersiones de aceite en agua. Adicionalmente, el modelo Euleriano-Euleriano logró predecir de forma aceptable los valores de holdup experimentales con un error promedio de 15.2%, mientras que las caídas de presión presentaron errores muy fluctuantes, llegando a alcanzar valores de hasta 428%.

---

[*] Trabajo de Grado

[**] Facultad de Ingenierías Fisicomecánicas. Escuela de Ingeniería Mecánica. Director: Octavio Andrés González Estrada, Doctor en Ingeniería Mecánica y de Materiales. Codirector: Germán González Silva, Doctor en Ingeniería Química.

Abstract

Title: Modeling of biphasic oil-water flow in horizontal pipes using CFD for the prediction of flow patterns[*]

Author(s): Santiago Hernández García[**]

Key Words: CFD, Oil-water flow, Flow pattern, Multiphase model

Description: A computational fluid dynamics study of the horizontal oil-water flow was performed using the Eulerian-Eulerian and mixture multiphase models in conjunction with the realizable k-ε turbulence model. The numerical models were carried out using water and mineral oil with a density of 880 kg/m^3 and a viscosity of 180 cP, varying the superficial velocities of both fluids in ranges of 0.1 – 1.2 m/s and 0.1 – 0.5 m/s, respectively. Under these conditions, entering the fluids in a mixed state, the stratified pattern could form adequately with the two multiphase models. Although the Eulerian-Eulerian model, together with the geometric reconstruction scheme, allowed us to visualize the three-dimensional dispersed patterns in a very similar way to the experimental results, the mixture model did not exhibit such similarity, especially in the oil-in-water dispersions. Additionally, the Eulerian-Eulerian model was able to acceptably predict the experimental holdup values with an average error of 15.2%, while the pressure drops showed highly fluctuating errors, reaching values of up to 428%.

---

[*] Degree Work

[**] Faculty of Physicomechanical Engineering. School of Mechanical Engineering. Director: Octavio Andrés González Estrada, PhD in Mechanical and Materials Engineering. Codirector: Germán González Silva, PhD in Chemical Engineering.

Introduction

Multiphase flows are present in industries such as the petrochemical, biochemical, and oil and gas. Many studies have been made on multiphase flows, but most of them focused on the interaction between liquid and gas through experimental analysis of water-air flows. Lately, the characterization of oil-water biphasic flow has increased interest in the search for improved transportation of off-shore oils. Unlike single-phase flow, when two or more phases flow simultaneously in a pipe or duct, the phases distribute in a particular way following certain flow patterns (Yadigaroglu & Hewitt, 2018), which influence the pressure drop (Abduvayt et al., 2006) and the heat transfer properties (Boostani et al., 2017; Hamidi et al., 2018) of the bulk flow.

There have been several attempts to identify oil-water flow patterns, but there is not yet a single set of patterns that have been universally obtained. Trallero et al. (1997) and Flores et al. (1999) carried out significant attempts to standardize the regimes of oil-water flow through horizontal and inclined pipes, respectively, including flow-pattern maps with superficial velocity coordinates that nowadays are still used as references. The oil-water flow through horizontal pipes was classified into six patterns (Trallero et al., 1997), stratified flow (ST), stratified with mixing in the interface (ST & MI), dispersion of oil in water and water (Do/w & w), dispersion of water in oil and oil in water (Dw/o & Do/w), emulsion of oil in water (o/w) and emulsion of water in oil (w/o). Moreover, Flores et al. observed that stratified flow was not present in experiments with inclination above 33° and classified the vertical flow patterns into two important types, water-dominated and oil-dominated patterns, and whether the dominating phase, there were observed three possible configurations of the discontinuous phase, very fine dispersion, dispersion in the shape of drops and churn flow. Despite the acceptance of these flow pattern categorizations, many

other flow patterns are observed in the literature, as Brauner (2003) mentioned, who reported eighteen possible flow patterns in horizontal systems. Also, a more comprehensive range of flow patterns could be developed depending on the oil viscosity and specific properties of the pipe's inner surface, like hydrophobic or hydrophilic behavior. Some studies have stated that the Eötvös number, the dimensionless number that quantifies the relationship between the gravitational forces and the surface tension forces, influences the development of certain flow patterns like slug/annular flow (Brauner, 2003) or bubbly flow (Al-Wahaibi et al., 2012).

One of the most interesting flow patterns is the core annular flow (CAF) because of its potential use in oil extraction, reducing the pressure drop. When the oil flows through a core in the inner of the pipe surrounded totally by the water flow, the minor viscosity of the water minimizes the resistance due to the contact with the pipe. Annular pattern formation is commonly aided by special injectors (Grassi et al., 2008), but it has also been observed in studies made with conventional tee mixers using high-viscosity oils (Sridhar et al., 2011).

Currently, to reduce processing times, the flow pattern prediction through flow pattern maps tends to be unused as it is impossible to integrate the viscosity and interfacial tension dependence in the pattern transitions in a simple way. Recent studies focused on the development of artificial neural networks (ANN) to predict diverse parameters of oil-water flow, such as the holdup (Ruiz-Diaz et al., 2021a, 2022), the pressure drop (Amooey, 2016; Azizi et al., 2016), and even the heat exchange (Boostani et al., 2017), through the input of determining input parameters like the superficial velocities of oil and water and relevant properties of the oil and the pipe. Wu et al. (2022) implemented a back-propagation neural network and a fuzzy inference system (FIS) to predict the flow pattern given the inclination, the total flow rate, and the water cut, and concluded that the predictions made by FIS were more accurate. However, the ANN can still use

the same training functions regardless of the number of training samples used, allowing further improvement of the predictions without changing the programming as FIS would need.

As the characterization of oil-water flow behavior tends to be predicted using ANN, the construction of a large reliable database that feeds the neural networks becomes more important and, despite the numerous experiments made in this area, they may still be insufficient to describe the influence of certain oil properties over a wide range (Ruiz-Diaz et al., 2021b). The numerical modeling of oil-water flow through CFD appears as an alternative to physical experimentation, allowing a more extensive dataset to be used as training samples for more accurate predictions of neural networks.

The greater flexibility in flow conditions that CFD allows is limited by the mathematical model used in the simulation (Cornejo Caceres et al., 2019). The Eulerian analysis of multiphase flows allows better capture of the interface between fluids, thus, models of this type are especially recommended for oil-water flows. Al-Yaari and Abu-Sharkh (2011) compared the prediction of the stratified pattern from three Eulerian multiphase models using the RNG k-ε turbulence model. They concluded that VOF (volume of fluid) is the one that most efficiently obtains an adequate interface between water and oil. Likewise, more recent studies (Bochio et al., 2021; Kang et al., 2021) have tested the VOF mathematical model in conjunction with different turbulence models to evaluate smooth (ST) and wavy (SW) stratified flow, and determined that acceptable interface profiles can be obtained, in addition to accurate pressure drop values and velocity profiles. However, the stratified pattern in oil-water flows is not the only one that can be observed from the VOF model. Desamala et al. (2014) also used this VOF model in a 2D simulation of mixing and development of the biphasic flow in horizontal pipes and were able to predict under certain conditions, not only stratified flow, but also other patterns such as annular, slug, and even early

signs of dispersion at the interface. In the attempt to model the core-annular flow in 3D, Shi et al. (2017, 2021) showed that the wall contact angle affected its formation by conventional mixing of the fluids. They concluded that, although the VOF model, in conjunction with the SST k-ω scheme, captures the annular interface well, it fails to accurately determine pressure drops, especially with highly viscous fluids.

Even when the VOF scheme shows as the most suitable approach to model oil-water flow patterns, it is not capable of satisfactorily simulating biphasic flow in a dispersed regime because it tends to require more refined grids to compensate for the smaller interface scales (Shi et al., 2017). Also, as it considers the mixture as a single fluid with variable composition, it ignores the interfacial forces originated by the interaction of a discrete phase in a continuous one. The Eulerian-Eulerian scheme, in which the balance equations are carried out for each phase separately, is the most used for flow simulations with a continuous and a dispersed phase because it has already been shown that, when integrating the different interfacial forces in their model, the distribution of the phases in the pipe resembles that observed experimentally (Walvekar et al., 2009). A constantly studied topic regarding dispersion in water-oil flows is the influence of interfacial forces, such as drag force, shear-lift force, virtual mass force, and turbulent dispersion force, on the accuracy of the model. Walvekar (2010) observed that in horizontal flow, the inclusion of the lift force and the turbulent dispersion force in the computational model did not significantly influence the radial distribution of the phases in the pipe, since drag was the determining force in the droplet distribution. On the other hand, Parvini et al. (2010) established that both lift and turbulent dispersion forces affected the vertical flow droplet distribution of dispersion in water-oil systems. In a similar work, Burlutskiy and Turangan (2015) used an

Eulerian-Lagrangian model in vertical flow configuration and obtained accurate pressure drop values by appropriately modeling the shear-lift force.

As could be noticed in the previously mentioned works, most of the oil-water flow CFD studies specialize in a certain flow pattern or, in their attempt to model different flow patterns, end up being limited in the modeling of dispersed flow. However, studies carried out with the Eulerian-Eulerian model have shown that it is capable of accurately characterizing the stratified flow in terms of phase distribution (Pouraria et al., 2016), pressure drop, and holdup (Rodriguez & Baldani, 2012), such that this multiphase model could be used to predict a great variety of existing patterns in the water-oil flow. In the present study, the horizontal oil-water flow is represented using the Eulerian-Eulerian and mixture multiphase models and the realizable k-ε turbulence model in a wide range of superficial velocities, in such a way that not only segregated flow patterns can be identified but also the cases in which, due to flow conditions, dispersed flow occurs.

1. Objectives

1.1 General Objective

Develop a water-oil flow model in CFD to accurately characterize the different flow patterns observed experimentally for a range of superficial fluid velocities.

1.2 Specific Objectives

Compare computational fluid dynamics models applied to multiphase and turbulent flows to determine the model that best fits all desired flow regimes.

Perform model preprocessing, optimizing the mesh and simulation parameters to minimize discretization and convergence errors in the solution.

Validate the model by comparing the results obtained in the simulation with experimental data regarding pressure drop, hold-up, and the observed flow pattern.

2. Methods and materials

The process followed for the development of the model consists of three fundamental parts, the evaluation and choice of the most suitable mathematical models to predict different flow patterns, the preprocessing and definition of the model, and, finally, the validation of the model by comparing the simulation results with pattern captures from oil-water flow experimentation. The required activities to complete each stage of the project are found in Figure 1.

Figure 1

Schematic representation of the activities required in the development of the project

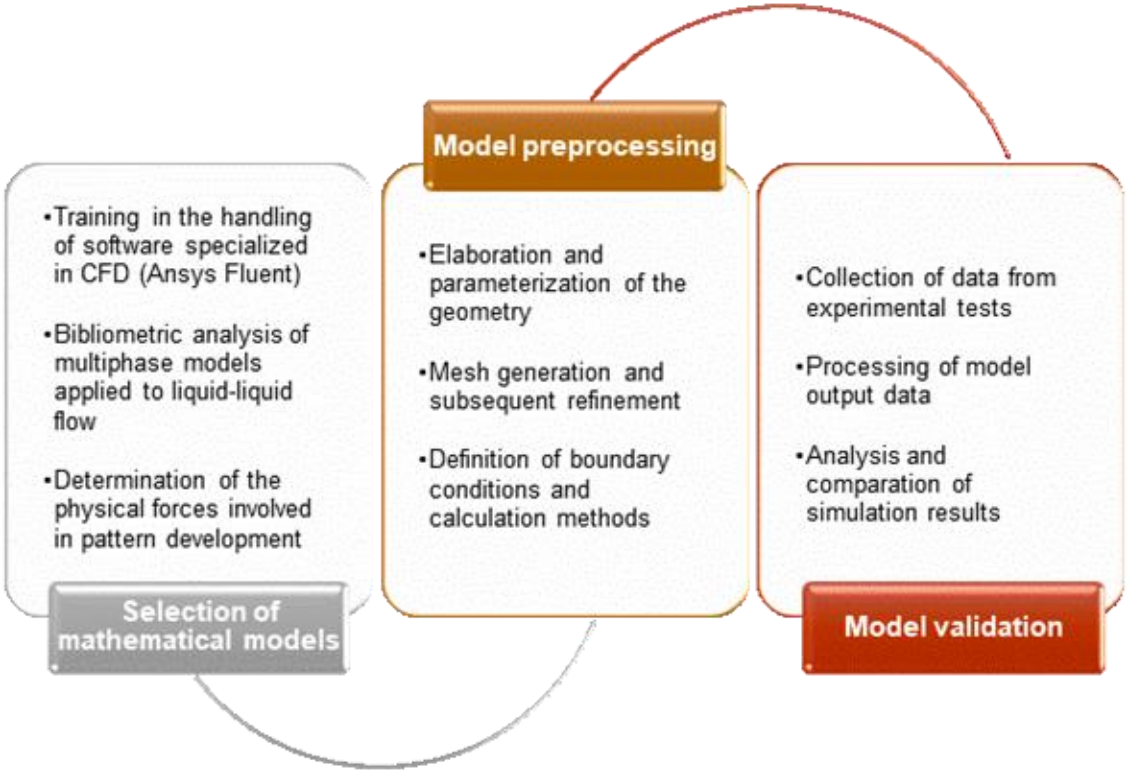

2.1 Mathematical model

2.1.1 Eulerian approach to multiphase flow

Multiphase models analyze the secondary phases either through an Eulerian or a Lagrangian approach. While the Lagrangian approach analyzes each discrete volume individually in such a way that the distribution of the involved phases is obtained by resolving the flow interaction with all the respective elements, the Eulerian models consider the entire medium as a continuous system, allowing the different phases to occupy the same position in space by making use of the concept of volume fraction (González Silva et al., 2018). An Eulerian approach is used to formulate the present CFD model, beginning with the comparison of two multiphase models that have shown to be capable of modeling the behavior of the flow in stratified and dispersed regimes, the mixture model and the Eulerian-Eulerian.

The main difference between the Eulerian models is presented in the way the velocity in each phase is calculated. Just as the VOF model is the simplest computationally since it considers that all the phases share the same velocity field, it also prevents widely studied effects in multiphase flow, such as slip ratio and interfacial forces, from showing up. On the other hand, the mixture model has the peculiarity that, although it solves a single Navier-Stokes equation in the momentum balance, it does not handle a single velocity profile for all phases. The continuity and momentum equations are applied to the entire mixture and are solved simultaneously to track the weight-averaged velocity $\mathbf{v_m}$, from which is obtained the specific velocity profile for each phase:

$$\frac{\partial}{\partial t}(\rho) + \boldsymbol{\nabla} \cdot (\rho \mathbf{v_m}) = 0 \tag{1}$$

$$\frac{\partial}{\partial t}(\rho \mathbf{v_m}) + \boldsymbol{\nabla} \cdot (\rho \mathbf{v_m} \mathbf{v_m}) = -\boldsymbol{\nabla} P + \boldsymbol{\nabla} \cdot [\mu(\boldsymbol{\nabla} \mathbf{v_m} + (\boldsymbol{\nabla} \mathbf{v_m})^{\mathrm{T}})] + \boldsymbol{\nabla} \cdot (\boldsymbol{\tau_{Dm}}) + \rho \mathbf{g} + \boldsymbol{S_M} \tag{2}$$

$$\mathbf{v_m} = \frac{\sum \alpha_i \rho_i \mathbf{v_i}}{\rho} \tag{3}$$

$$\rho = \sum \alpha_i \rho_i \, ; \quad \mu = \sum \alpha_i \mu_i \tag{4}$$

Where α_i, ρ_i and μ_i are the volume fraction, density, and viscosity of a singular phase i, and ρ and μ are the mixture properties, obtained as a volume-fraction average of individual phases properties, as shown in Equation (4). The vector $\mathbf{S_M}$, in Equation (2), represents the sum of all possible external sources of momentum per unit volume, while the stress tensor $\boldsymbol{\tau}_{\mathbf{Dm}}$ contains the diffusion stresses due to phase slip and depends on the drift velocities $\mathbf{v_{dr,i}}$, that relate the individual velocities $\mathbf{v_i}$ to the average velocity as expressed below:

$$\mathbf{v_{dr,i}} = \mathbf{v_i} - \mathbf{v_m} \tag{5}$$

$$\boldsymbol{\tau}_{\mathbf{Dm}} = \sum \alpha_i \rho_i \mathbf{v_{dr,i}} \mathbf{v_{dr,i}} \tag{6}$$

Physically, the drift velocities are not as decisive in the interaction between phases as the relative (slip) velocities. Therefore, through simplifications of the momentum equation for each secondary phase j, the respective slip velocities relative to the primary phase k can be determined. The drift velocities can be calculated by knowing the slip velocities of all the secondary phases, as shown in Equation (7).

$$\mathbf{v_{dr,j}} = \mathbf{v_{jk}} - \sum_{i \neq j}^{n} \frac{\alpha_i \rho_i \mathbf{v_{ik}}}{\rho} \tag{7}$$

$$\mathbf{v_{ik}} = \mathbf{v_i} - \mathbf{v_k} = \frac{4 d_i}{3 C_D |\mathbf{v_m}|} \left(\frac{\rho_i - \rho}{\rho_k} \right) \left[\mathbf{g} - (\mathbf{v_m} \cdot \boldsymbol{\nabla}) \mathbf{v_m} - \frac{\partial \mathbf{v_m}}{\partial t} \right] - \left[\frac{\eta_t}{\sigma_t} \left(\frac{\boldsymbol{\nabla} \alpha_i}{\alpha_i} - \frac{\boldsymbol{\nabla} \alpha_k}{\alpha_k} \right) \right] \tag{8}$$

The expression to obtain the relative velocities $\mathbf{v_{ik}}$, shown in Equation (8), includes some interfacial flow phenomena to the model, as the first term of this expression represents the

relationship between the relative velocity and drag, and the second term includes the effect of diffusion due to turbulent fluctuations.

To track the composition through the flow, the mixture model requires as many continuity equations as the number of phases, and, in addition to the mixture continuity equation, a volume fraction equation is used for each secondary phase, deduced from the differential mass balance of these phases individually.

$$\frac{\partial}{\partial t}(\alpha_i \rho_i) + \boldsymbol{\nabla} \cdot (\alpha_i \rho_i \mathbf{v_m}) = S_{\alpha,i} - \boldsymbol{\nabla} \cdot \left(\alpha_i \rho_i \mathbf{v_{dr,i}}\right) \tag{9}$$

Where $S_{\alpha,i}$ accounts for any volumetric source of the phase mass. Finally, the Eulerian-Eulerian model is more complex since it performs the mass and momentum balance for each component separately, which requires the discretization of additional momentum equations and, in addition to keeping track of the volume fractions, tracks a specific velocity profile for each phase ($\mathbf{v_i}$). In this way, for each phase in a multiphase flow without mass transfer, the conservation equations yield:

$$\frac{\partial}{\partial t}(\alpha_i \rho_i) + \boldsymbol{\nabla} \cdot (\alpha_i \rho_i \mathbf{v_i}) = S_{\alpha,i} \tag{10}$$

$$\frac{\partial}{\partial t}(\alpha_i \rho_i \mathbf{v_i}) + \boldsymbol{\nabla} \cdot (\alpha_i \rho_i \mathbf{v_i v_i}) = -\alpha_i \boldsymbol{\nabla} P + \boldsymbol{\nabla} \cdot (\boldsymbol{\tau_i}) + \alpha_i \rho_i \mathbf{g} + \mathbf{F_{int,i}} + \mathbf{S_{M,i}} \tag{11}$$

$$\mathbf{F_{int,i}} = \mathbf{F_{drag,i}} + \mathbf{F_{lift,i}} + \mathbf{F_{wl,i}} + \mathbf{F_{vm,i}} + \mathbf{F_{td,i}} \tag{12}$$

Where $\mathbf{F_{int,i}}$ is the sum of all interfacial forces, including drag force, shear-lift force, wall lubrication force, virtual mass force, and turbulent dispersion force. $\mathbf{S_{M,i}}$ represents any phasic volumetric source of moment due to the action of external forces and $\boldsymbol{\tau_i}$ is the viscous stress tensor produced in each phase, which is determined as follows for incompressible fluids:

$$\boldsymbol{\tau_i} = \alpha_i \mu_i (\boldsymbol{\nabla v_i} + (\boldsymbol{\nabla v_i})^{\mathrm{T}}) \tag{13}$$

As for the interfacial forces, each one has a respective mathematical model. The drag force is the most determinant in horizontal liquid-liquid flow, not only in the distribution of drops in the dispersed pattern but also in the formation of drops in the pattern transition (Al-Wahaibi et al., 2007). Expressions to calculate the drag force in droplets are shown in Equation (14), where C_D is the drag coefficient, d_i is the droplet diameter, a_{int} is the interfacial area concentration, and the density is evaluated in the continuous phase k.

$$\mathbf{F_{drag,i}} = \frac{3}{4}\frac{C_D \rho_k \alpha_i}{d_i}|\mathbf{v_k} - \mathbf{v_i}|(\mathbf{v_k} - \mathbf{v_i}) = \frac{C_D \rho_k a_{int}}{8}|\mathbf{v_k} - \mathbf{v_i}|(\mathbf{v_k} - \mathbf{v_i}) \tag{14}$$

Research in recent decades has focused on developing adequate correlations of the drag coefficient. However, most works have opted to generalize the drag of fluid dispersed elements based on the interaction of air bubbles in the water. Although not many works focused on the dispersion of droplets in a liquid matrix have succeeded in obtaining the drag coefficient for a wide variety of flow conditions, the use of specific correlations of liquid-liquid flow allows getting better results in CFD modeling of oil-water dispersion (Walvekar, 2010). The Rusche and Issa (2000) work is the latest attempt to correlate the drag coefficient for a wide variety of fluids and flow conditions, obtaining the expression in Equation (15) for droplet dispersion drag in a liquid medium.

$$C_D = C_{D0}(\exp(2.1\alpha_i) + \alpha_i^{0.249}) \tag{15}$$

$$C_{D0} = \begin{cases} \frac{24}{Re}(1 + 0.15Re^{0.687}) & Re \equiv \frac{\rho_k d_i |\mathbf{v_k} - \mathbf{v_i}|}{\mu_k} \leq 1000 \\ 0.44 & Re \equiv \frac{\rho_k d_i |\mathbf{v_k} - \mathbf{v_i}|}{\mu_k} > 1000 \end{cases} \tag{16}$$

The other interfacial forces must be interpreted carefully as their influence may vary depending on the case studied. For instance, the virtual mass force $\mathbf{F_{vm}}$ is presented by the effect of inertia that the particulate elements perceive when trying to accelerate with respect to the continuous phase, as represented in Equation (17). However, when evaluating a continuous flow through a pipe, this force is not significant and is not worth including in the model unless the dispersed phase is much less dense.

$$\mathbf{F_{vm,i}} = 0.5\rho_k\alpha_i\left(\frac{\mathrm{D}}{\mathrm{D}t}(\mathbf{v_k}) - \frac{\mathrm{D}}{\mathrm{D}t}(\mathbf{v_i})\right) \tag{17}$$

Another case is that of lift, wall-lubrication, and turbulent dispersion forces since these are mainly radial forces. The lift force $\mathbf{F_{lift}}$ is produced by the net effect of the stresses generated on the surface of the particle due to the variation of the speed in the medium, as expressed in Equation (18). However, as none of the numerical models for the C_L coefficient value is fully reliable for bubbles or droplets, the value of 0.5, valid for inviscid flow, tends to be used in the CFD models. The wall-lubrication force ($\mathbf{F_{wl}}$) tends to push the dispersed material inside the pipe, being responsible for generating a thin layer of fluid free of particles in the vicinity of the walls, while the turbulent dispersion force ($\mathbf{F_{td}}$) tends to homogenize the distribution of dispersed material. The effect of these forces has been studied mostly on bubble column flow because, in dispersed horizontal flow, the net force in the radial direction is also affected by buoyancy. In this way, it has been observed in the oil-water flow that the action of lift and turbulent dispersion has minimum effect on the distribution of drops in horizontal flow (Walvekar, 2010), while wall lubrication tends to be effective for a layer of thickness comparable to a drop diameter (Rodriguez et al., 2019), so they become irrelevant in the present model, whose objective is to identify the different patterns in flows of this nature.

$$\mathbf{F_{lift,i}} = -C_L \rho_k \alpha_i (\mathbf{v_k} - \mathbf{v_i}) \times (\boldsymbol{\nabla} \times \mathbf{v_k}) \tag{18}$$

$$\mathbf{F_{wl,i}} = -\frac{C_{wl} \rho_k \alpha_i}{d_i} |(\mathbf{v_k} - \mathbf{v_i}) \cdot \hat{\mathbf{n}}_\mathbf{z}|^2 \, \hat{\mathbf{n}}_\mathbf{r} \tag{19}$$

$$\mathbf{F_{td,i}} = -C_{TD} (C_D A_{int} |\mathbf{v_k} - \mathbf{v_i}|) \frac{\eta_t}{\sigma_{ik}} \left(\frac{\boldsymbol{\nabla} \alpha_i}{\alpha_i} - \frac{\boldsymbol{\nabla} \alpha_k}{\alpha_k} \right) \tag{20}$$

2.1.2 Interfacial area concentration

The multiphase models studied can handle dispersed phases as long as the particle diameter is known, a determining property in the calculation of interfacial forces. When analyzing the dispersed regimes in liquid-liquid flow, the dispersed fluid is divided into drops due to the high energy present in the medium, mainly due to turbulence. Brauner (2001) applied the critical Weber number to deduce the maximum diameter to maintain a dispersed droplet in the flow without breaking and established a critical diameter over which the dispersed phase is not maintained naturally, managing to precisely predict the pattern transition from stratified to dispersed.

$$\frac{d_{max}}{D} = 7.61 We_c^{-0.6} Re_c^{0.08} \left(\frac{\epsilon_d}{\epsilon_c} \right)^{0.6} \left(1 + \frac{\rho_d \epsilon_d}{\rho_c \epsilon_c} \right)^{-0.4} \tag{21}$$

$$d_{max} \cong 7.61 D \left(\frac{\rho_c D}{\mu_c \sigma} \right)^{-0.52} \left(\frac{\sigma^{0.08}}{\mu_c^{0.6}} \right) \left(\frac{J_d}{J_c * (J_d + J_c)^{1.12}} \right) \left(1 + \frac{\rho_d J_d}{\rho_c J_c} \right)^{-0.4} \tag{22}$$

Where We is the Weber number, ϵ is the holdup, J is the superficial velocity, and the subscripts c and d represent the continuous and dispersed phase, respectively. Although the particle diameter is ideal for characterizing a completely dispersed material, since there is the possibility that the secondary phase flows as a continuum, it is more convenient to work with the interfacial area concentration, which can be modified in such a way that it identifies the dispersion-

free zones. Equation (23) shows the conventional expression for the interfacial area concentration in flows strictly composed of a continuous phase and a spherical shape dispersed phase.

$$a_{int} = \frac{A_{int}}{V}\frac{\alpha_i}{\alpha_i} = \frac{\alpha_i\,(\pi d_i^{\,2})}{(\pi d_i^{\,3}/6)} = \frac{6\alpha_i}{d_i} \tag{23}$$

The assumption of spherical shape is also applicable to droplet dispersion, but due to liquid phases' ability to present as continuous media, the symmetry model tends to be used for the calculation of interfacial area concentration in liquid-liquid flow, because it modifies the original expression so that the concentration can take the value of zero in case any of the two phases present a volume fraction equals to 1.

$$a_{int} = \frac{6\alpha_i(1-\alpha_i)}{d_i} \tag{24}$$

2.1.3 Turbulence model

The realizable *k-ε* turbulence model, applied to this work, is a variation of the conventional *k-ε* model that applies corrections to the former one, aiming to ensure it is realizable even in regions of high mean strain rate. Models of this type, like the also widely known *k-ω* model and its variations, are known as Reynolds averaged methods because, to consider the fluctuations generated by turbulence, the flow velocity is separated into two components, an average velocity field $\bar{\mathbf{v}}$ and the fluctuating velocity $\mathbf{v}'$, which when replaced in the momentum balance equation, results in an equation known as Reynolds Averaged Navier-Stokes (RANS), shown in Equation (25), very similar to the conventional Navier-Stokes equation, but with the appearance of an additional variable known as Reynolds-stress tensor $\boldsymbol{\tau}^{\mathbf{R}}$. At the physical level, the existence of this tensor is due to the presence of turbulent fluctuations, unlike the other terms, expressed as

functions of the average velocity, so for the full development of the equation it is necessary to approximate this tensor in terms of the average velocity through expressions known as closure relations.

$$\frac{\partial}{\partial t}(\rho\bar{\mathbf{v}}) + \boldsymbol{\nabla}\cdot(\rho\bar{\mathbf{v}}\bar{\mathbf{v}}) = -\boldsymbol{\nabla}P + \boldsymbol{\nabla}\cdot[\mu(\boldsymbol{\nabla}\bar{\mathbf{v}} + (\boldsymbol{\nabla}\bar{\mathbf{v}})^{\mathrm{T}})] + \boldsymbol{\nabla}\cdot(\boldsymbol{\tau}^{\mathbf{R}}) + \rho\mathbf{g} + \boldsymbol{S}_{\mathbf{M}} \tag{25}$$

$$\tau_{ij}^{R} = -\rho\overline{v_i' v_j'} \cong \mu_t\left(\frac{\partial\overline{v}_i}{\partial x_j} + \frac{\partial\overline{v}_j}{\partial x_i}\right) - \frac{2}{3}\rho\delta_{ij}k \tag{26}$$

The simplest complete turbulence models work with closure relations using an eddy-viscosity (μ_t) approximation, as seen in Equation (26), and their research is based on finding the most suitable way to model this turbulent viscosity from the turbulent kinetic energy (k) and its dissipation into thermal energy. While the *k-ω* turbulence models handle a specific variable for dissipation rate (ω), the *k-ε* equations keep track of the total turbulence dissipation rate (ε), determining the eddy-viscosity as shown below.

$$\mu_t = \rho C_\mu \frac{k^2}{\varepsilon} \tag{27}$$

Where C_μ is a constant equal to 0.09 in the conventional *k-ε* model. However, the main modification that Shih et al. (1995) implemented to make the model realizable was to convert this constant into a variable whose value depends on the mean strain rate (**S**) and mean rotation rate ($\boldsymbol{\Omega}$) tensors. The variable C_μ ends up being determined as follows.

$$C_\mu = \frac{1}{4.04 + \sqrt{6}\cos(\varphi)\,U^*\frac{k}{\varepsilon}} \tag{28}$$

$$U^* = \sqrt{S_{ij}S_{ij} + \Omega_{ij}\Omega_{ij}}\,, \qquad \varphi = \frac{1}{3}\arccos\left(\sqrt{6}W\right)\,, \qquad W = \frac{S_{ij}S_{jk}S_{ki}}{\tilde{S}^3} \tag{29}$$

$$S_{ij} = \frac{1}{2}\left(\frac{\partial \overline{v}_i}{\partial x_j} + \frac{\partial \overline{v}_j}{\partial x_i}\right), \qquad \Omega_{ij} = \frac{1}{2}\left(\frac{\partial \overline{v}_i}{\partial x_j} - \frac{\partial \overline{v}_j}{\partial x_i}\right) \tag{30}$$

To finish determining the effect of turbulence along the flow, the two characteristic model variables (k and ε) are tracked following their balance equations and are solved simultaneously with the mass and momentum conservation equations. These turbulence governing equations are expressed in Equation (31) and Equation (32).

$$\frac{\mathrm{D}(\rho k)}{\mathrm{D}t} \equiv \frac{\partial(\rho k)}{\partial t} + \boldsymbol{\nabla}\cdot(\rho k\mathbf{v}) = \boldsymbol{\nabla}\cdot\left(\left(\mu + \frac{\mu_t}{\sigma_k}\right)\boldsymbol{\nabla}k\right) + (\boldsymbol{\tau}^{\mathbf{R}}\!:\mathbf{S}) - \rho\varepsilon \tag{31}$$

$$\frac{\mathrm{D}(\rho \varepsilon)}{\mathrm{D}t} \equiv \frac{\partial(\rho \varepsilon)}{\partial t} + \boldsymbol{\nabla}\cdot(\rho \varepsilon\mathbf{v}) = \boldsymbol{\nabla}\cdot\left(\left(\mu + \frac{\mu_t}{\sigma_\varepsilon}\right)\boldsymbol{\nabla}\varepsilon\right) + \rho C_1 \bar{S}\varepsilon - \rho C_2 \frac{\varepsilon^2}{k + \sqrt{\nu\varepsilon}} \tag{32}$$

$$C_1 = \max\left[0.43, \frac{\eta}{\eta + 5}\right], \qquad \eta = \frac{\bar{S}k}{\varepsilon} \tag{33}$$

Where $C_2 = 1.9$, $\sigma_k = 1$ and $\sigma_\varepsilon = 1.2$, while the variables $\bar{S}$ and $\tilde{S}$ represent the mean and the RMS strain rate, respectively, calculated as shown in Equation (34):

$$\bar{S} = \sqrt{2S_{ij}S_{ij}}, \qquad \tilde{S} = \sqrt{S_{ij}S_{ij}} \tag{34}$$

2.2 Numerical model and mesh generation

The oil-water flow modeling is fully programmed in Ansys Workbench (see Appendix A). In this software, the geometry used consists of a 0.025 meters internal diameter horizontal pipe. It is assumed that the flow enters completely mixed as an emulsion but without sliding between phases, in such a way that the inlet volume fraction and velocity of each fluid can be determined from the superficial velocities.

$$V_w = V_o = J_w + J_o \tag{35}$$

$$\epsilon_w = \frac{A_w}{A} = \frac{J_w}{J_w + J_o}\ ; \qquad \epsilon_o = \frac{A_o}{A} = \frac{J_o}{J_w + J_o} \tag{36}$$

Where J_w and J_o are the superficial velocities of water and oil, respectively, and ϵ_w and ϵ_o are the holdups at the inlet, equivalent to the respective volume fractions. Additionally, to finish determining the system, the wall boundary condition is defined for the lateral face of the cylinder and null gauge pressure for the outlet section.

The model pipe has a length of 1.5 m, enough to allow the development of the pattern. For the mesh, an O-H structured mesh is used in the input section and extended through the pipe length. The resulting mesh, as shown in Figure 2, consists of only hexahedral elements with a slight refinement in the area near the wall.

Figure 2

Generated mesh for the model geometry

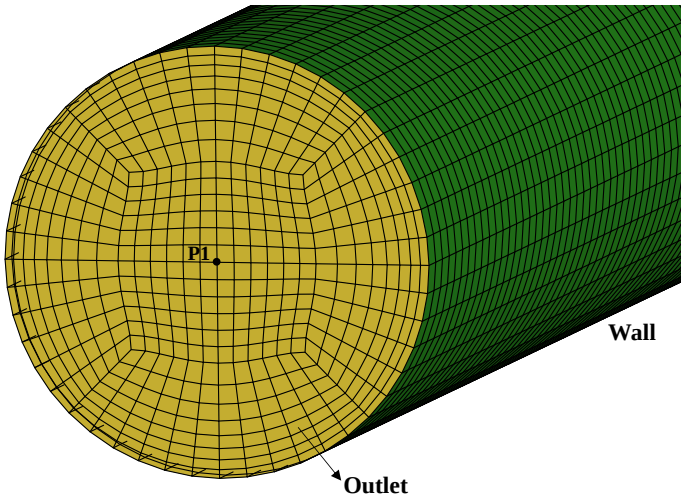

The transient flow was solved using mixture and Eulerian-Eulerian multiphase models with the inclusion of drag as the only interface interaction force, using the Rusche-Issa correlation in Ansys Fluent (ANSYS Inc, 2021). The realizable *k*-ε turbulence model is used with an initial turbulence intensity calculated according to the expression in Equation (37). For the resolution of the system, the QUICK second-order scheme is used for the discretization of the field variables, and the SIMPLE and PC-SIMPLE algorithms are selected for the pressure-velocity coupling in the mixture and Eulerian-Eulerian models, respectively.

$$I_t = 0.16Re^{-1/8}\,; \qquad k_0 = \frac{3}{2}(I_t|\mathbf{v_0}|)^2 \tag{37}$$

2.3 Experimental setup

The experimental patterns used for the validation of the model were obtained in the experimental bench of the Industrial Multiphase Flow Laboratory (LEMI) of the Sao Carlos School of Engineering from University of Sao Paulo (Hernández-Cely & Ruiz-Diaz, 2020). The assembly of the equipment on this bench, schematized in Figure 3, besides achieving the mixing of water and oil flows through a Y joint, allows accurate measurements of average holdups and the capture of phase distribution in the cross-section employing a wire mesh sensor (WMS).

In the experiments, water with a viscosity of 1 cP and a density of 997 kg/m^3 and LUBRAX Turbine 100 mineral oil with a viscosity of 180 cP and a density of 880 kg/m^3 were used. The borosilicate pipe to visualize the patterns was kept horizontal in all the experiments and had dimensions of 12 m long and 25.4 mm internal diameter.

Regarding the flows to handle, experiments were carried out by varying the superficial velocities of both fluids, water in a range of 0.1 to 1.2 m/s and oil in a range of 0.1 to 0.5 m/s, selecting the conditions in which the different patterns are most clearly identified.

Figure 3

Schematic representation of the equipment used in the LEMI experimental bench

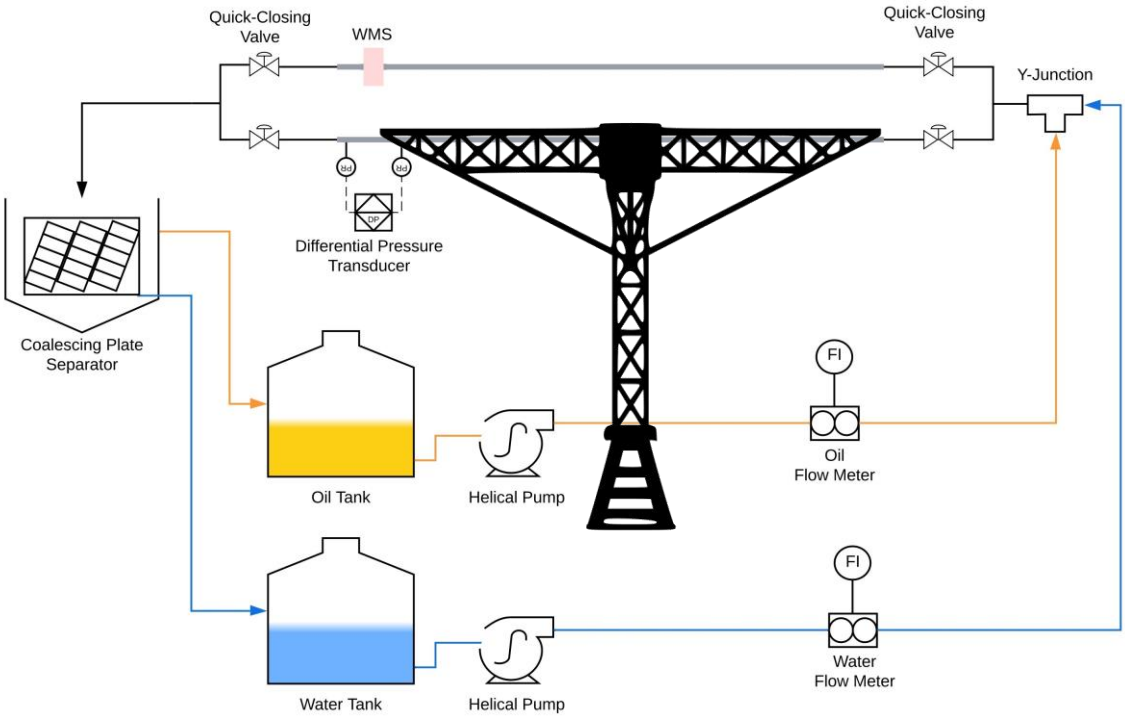

Note. Adapted from (Hernández-Cely & Ruiz-Diaz, 2020)

3. Results

3.1 Mesh independence test

For the mesh independence test, six different meshes are generated through uniform refinements in the entire volume, increasing the number of elements between 1.5 and 3 times. Table 1 shows the number of elements in each mesh, using the axial velocity at the center of the

outlet section as the analysis variable. The error is calculated as the relative error between the velocities obtained in each distribution and the immediate coarser mesh. The simulations are performed using the Eulerian-Eulerian model with superficial velocities of 0.915 m/s and 0.309 m/s for water and oil, respectively, for a flow time of 3.5 seconds.

Table 1

Meshes in the mesh sensitivity analysis

Mesh	Number of Cells	Axial Vel. (m/s)	Error (%)
A	24000	1.509	–
B	70200	1.532	1.53
C	153600	1.504	1.82
D	285000	1.572	4.51
E	475200	1.589	1.11
F	735000	1.598	0.56

As noted in Table 1, the relative error is kept low in all meshes, but comparing the axial velocities, as finer meshes are used, the velocity tends to stabilize at a value close to 1.6 m/s. The variation of velocity with the increase in the number of elements may be better observed in Figure 4, from which Mesh E (475200 cells) is selected since the improvement in accuracy obtained with the subsequent refinement is not significant considering the increase in computational cost required by the model.

Figure 4

Variation of axial velocity with the number of elements of the study meshes

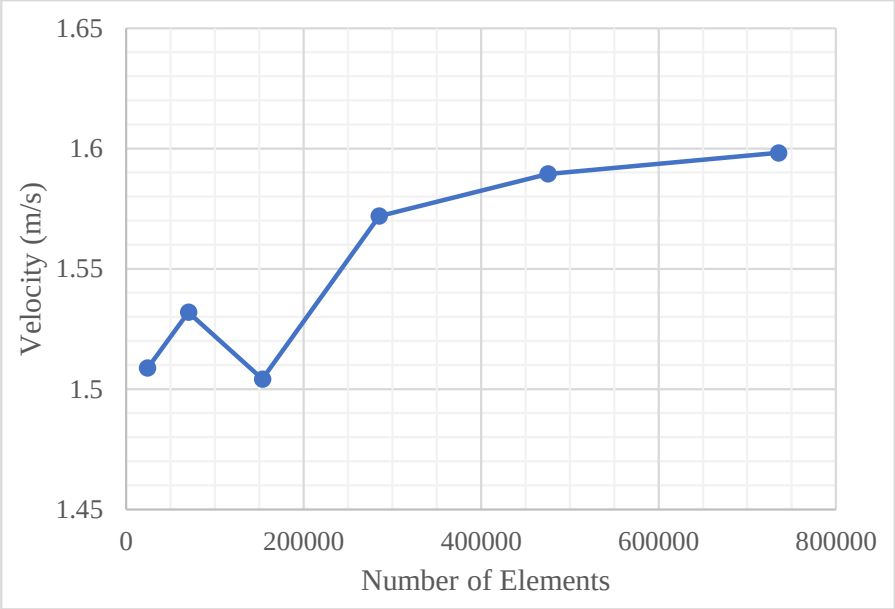

3.2 Model validation

For validation of the model, experimental data obtained by Hernández-Cely and Ruiz-Diaz (2020) are used, with a set of seven cases having six different flow patterns, to evaluate the robustness of the model when predicting the patterns. The operational conditions in which the reference patterns were developed are found in Table 2.

The inlet condition forces the flow to enter as a uniform dispersion, for which the phase with the lowest surface velocity is considered as the dispersed fluid, modeled from the symmetric interfacial area concentration model with the droplet size based on the maximum diameter estimated by Brauner (2001), but limited to a maximum value of $0.1D$.

Table 2

Selected experimental tests for model validation

Experiment	J_w (m/s)	J_o (m/s)	Observed Pattern
1	0.104	0.1	ST
2	0.304	0.215	ST & MI
3	0.724	0.223	Do/w & w
4	0.915	0.309	Do/w & w
5	1.106	0.115	Do/w
6	0.313	0.411	Dw/o & o
7	0.107	0.404	Dw/o

The three-dimensional visualization of simulated patterns is performed in the final section of the model pipe, capturing the interface through volume fraction iso-surfaces. According to the simulations at the flow conditions implemented in Experiment 1, shown in Figure 5, in both the mixture model and the Eulerian-Eulerian model, a stratified flow development similar to that developed experimentally is observed, with the difference that the Eulerian-Eulerian model generates more disturbances on the surface of the interface, more closely resembling the small waves observed experimentally. Something important to highlight from this experiment is that, despite the volumetric flows of both fluids being very similar, the oil shows some stagnation due to its high viscosity compared to water. Therefore, an increase in the area occupied by oil is observed, which could also be observed in the respective simulations.

Figure 5

Comparison between experimental and simulated flow configurations obtained at Experiment 1 conditions

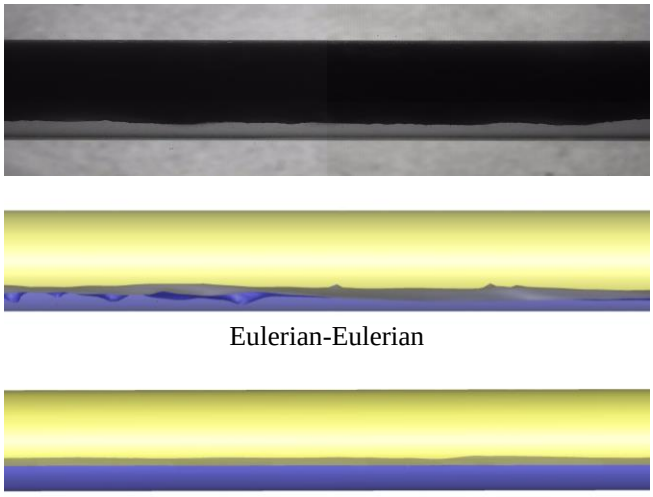

Eulerian-Eulerian

Mixture

Although capturing the interface in separated flow is quite simple, in the case of dispersed flow, multiphase models relate the number of droplets present in any control volume to the respective volume fraction, making the formation of closed boundaries for particulate elements unnecessary since these are implicit in the volume fraction calculation. As seen in the longitudinal sections shown in Figure 6, the dispersed flow differs from the separated one due to the slight transition between phases, since the wide zone of intermediate volume fraction implies the presence of dispersed elements in that area.

Figure 6

Difference in the phase distribution of separated and dispersed flows

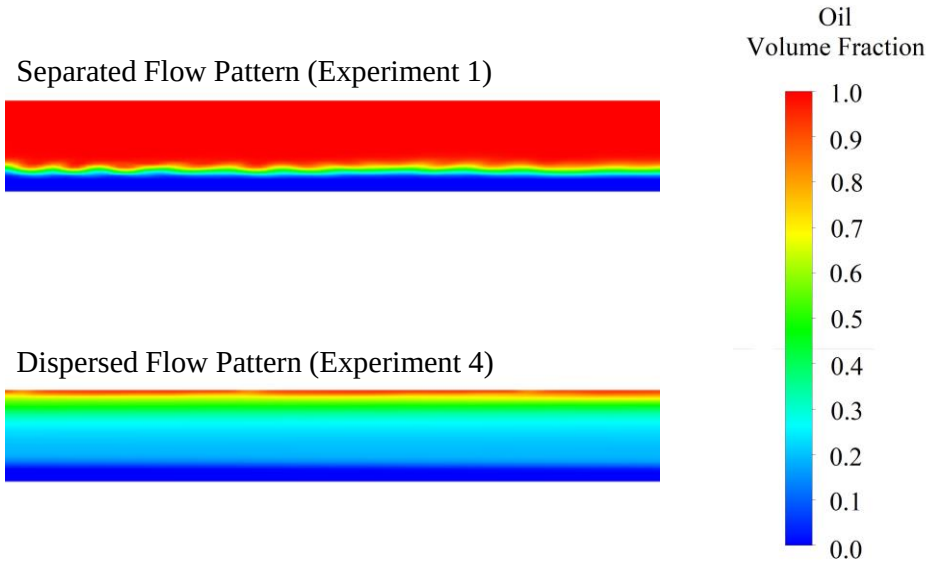

The Youngs' geometric reconstruction scheme is a useful method to achieve more accurate interface tracking, forcing an explicit separation of the phases within the control volumes according to the cell volume fraction and the fluxes to neighboring cells (Rudman, 1997). In this way, using this scheme as a final treatment in dispersed flows facilitates the visualization of the droplets as they are distinguished in the experimental captures. Figure 7 shows the difference in phase separation when using the geometric reconstruction scheme in the simulated disperse pattern under the conditions of Experiment 4.

Figure 7

Variation in interface tracking using the geometric reconstruction scheme

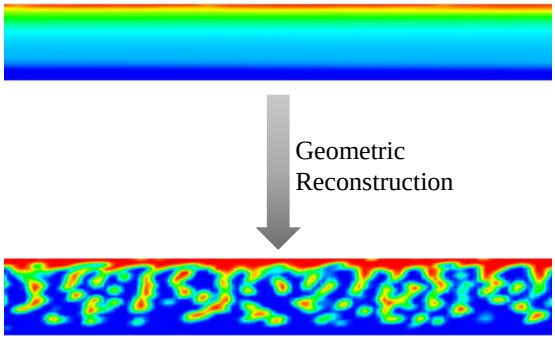

Using the geometric reconstruction scheme in the subsequent analyzes contributes to achieving an adequate visualization of the dispersed patterns in 3D. In Experiments 2 and 3, shown in Figure 8, it is possible to differentiate the greater separation of drops from the oil continuum by increasing the flow of water, which is replicated in a similar way in the computational simulations. However, in both cases, the mixture model tends to show less dispersion compared to experimental patterns and obtained with the Eulerian-Eulerian model.

Figure 8

Comparison between experimental and simulated flow configurations: a) Experiment 2, b) Experiment 3

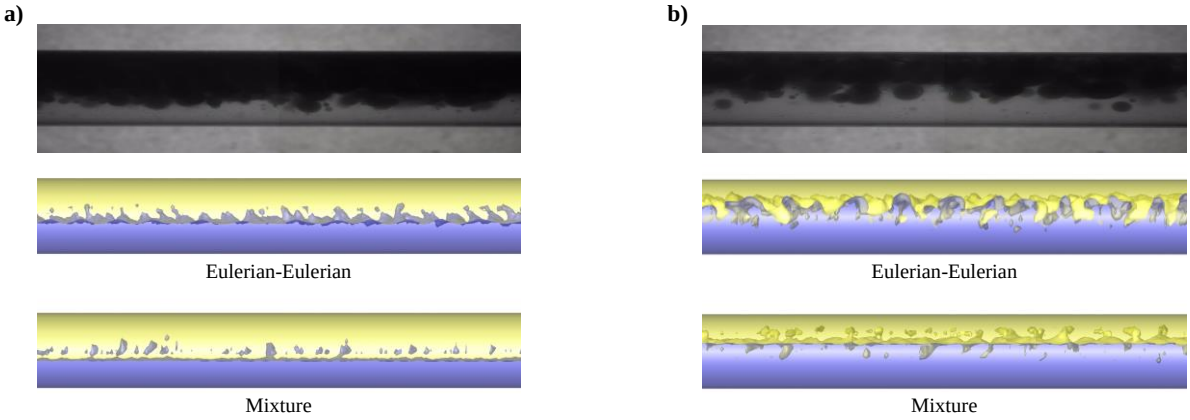

Figure 9 shows the experimental and simulated results of the cases of dispersion of oil in water, observed in Experiments 4 and 5, in which some differences can be noted when using the mixture model, especially in Experiment 4, since the flow pattern obtained using this model seems to be stratified with mixing in the interface (ST&MI) with little oil dispersion, contrary to the experimental pattern. On the other hand, the Eulerian-Eulerian model seems to accurately simulate the patterns in both cases, noting the dispersion of oil droplets in the aqueous medium and emulating their tendency to concentrate in the upper part of the pipe.

Figure 9

Comparison between experimental and simulated flow configurations for oil-in-water dispersions: a) Experiment 4, b) Experiment 5

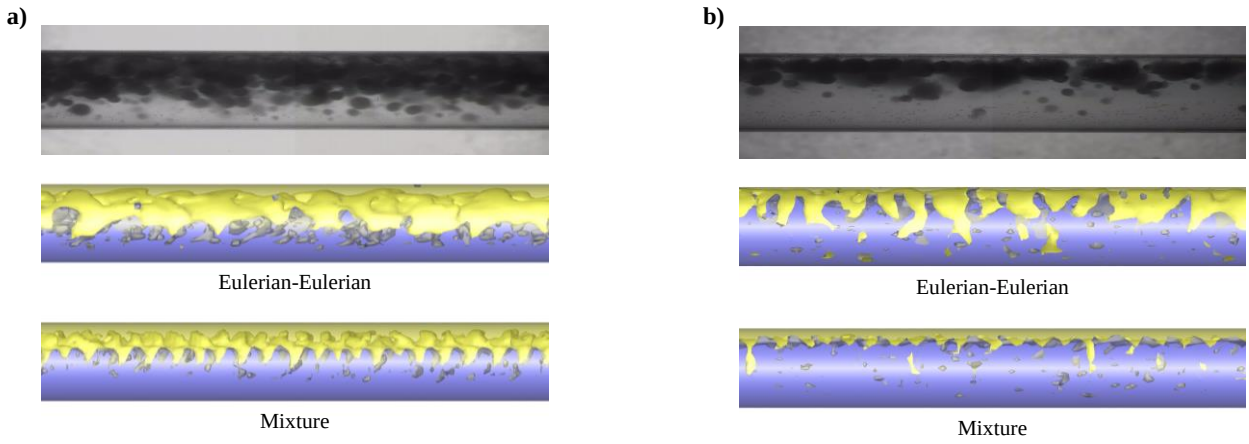

The simulated flow configurations of water-in-oil dispersions are shown in Figure 10, where it is observed that the model effectively shows the total dispersion of water in the oil in both cases. However, the comparison between the images is limited by the fact that the experimental

shots only highlight the oil, which means that the drops of water dispersed inside the oil are not observable.

Figure 10

Comparison between experimental and simulated flow configurations for water-in-oil dispersions: a) Experiment 6; b) Experiment 7

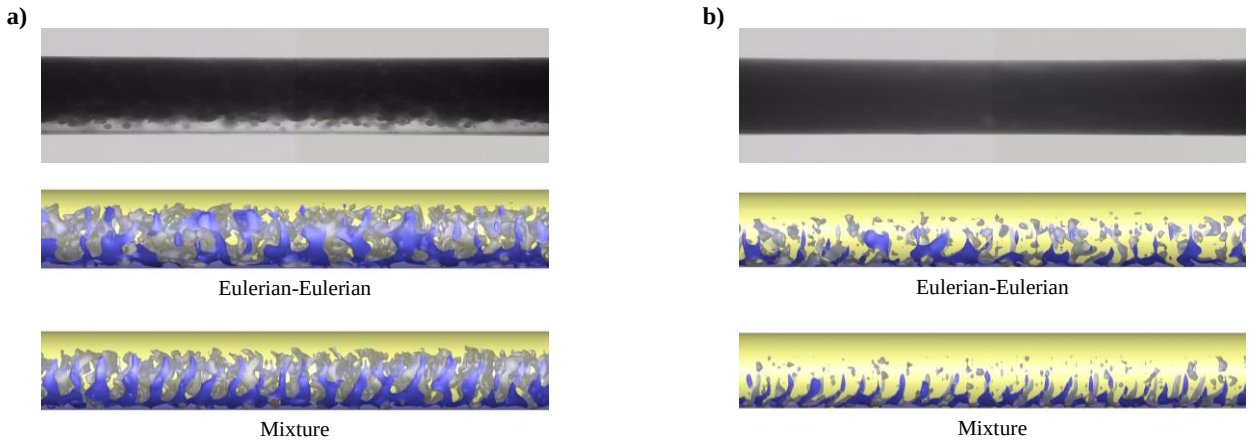

Although all the water is dispersed in the computational results of Experiment 7, a dispersion-free oil layer is observed with the two multiphase models, which was not expected to be obtained according to the flow pattern reported when performing the experimental tests (Dwo).

3.2.1 Comparison with experimental data

The simulated cases using the Eulerian-Eulerian model are compared to the experimental data of holdup and pressure drop. The results, summarized in Table 3, do not fit in a general way in all the experiments as in the works of Shi et al. (2017, 2021). While the holdup results show adequate accuracy, since the model tends to underpredict this variable with a maximum error of

32% among all the cases, when evaluating the pressure drop, only one case presents an error of less than 30%. Experiment 1 is the only representative of the stratified flow pattern, the one with the least discrepancy.

Table 3

Comparison of experimental and computational pressure gradients and holdups

Experiment	Flow Pattern	dP/dz (Pa m^{-1})			Water holdup		
		Exp.	CFD	Error (%)	Exp.	CFD	Error (%)
1	ST	884	787.1	10.96	0.385	0.256	33.51
2	ST & MI	2813	1956.2	30.46	0.462	0.405	12.34
3	Do/w & w	2318	3257.3	40.52	0.738	0.654	11.38
4	Do/w & w	3005	4899.1	63.03	0.818	0.677	17.24
5	Do/w	869	4595.3	428.8	0.939	0.842	10.33
6	Dw/o & o	3266	5301.4	62.32	0.385	0.377	2.08
7	Dw/o	6820	4838.0	29.06	0.154	0.184	19.48

On the other hand, the accuracy of the pressure drop results in dispersed flow patterns shows to be very irregular, with errors ranging between 30% and 428%. It is also to be noted that between experiments 4 and 5, which handle the same total flow of 600 mL/s, the experimental pressure gradient drops significantly with a slight decrease in the oil composition at the inlet. The most reasonable explanation for this phenomenon is found in the distribution of the dispersed phase, since in experiment 5, the capture shows that the dispersed phase does not come into contact with the pipe wall, which would explain why the pressure gradient was so similar to that obtained when only water flows using the same flow rate (dP/dz = 647.5 Pa/m). The CFD simulation, despite obtaining a similar degree of dispersion, by considering buoyancy as the only radial force to which the drops are exposed, has no way of avoiding contact between the oil and the pipe, resulting in higher pressure drops in oil-in-water dispersions.

4. Conclusions

The results obtained with the Eulerian-Eulerian multiphase model and the realizable k-ε turbulence model showed that the use of CFD allows simulating with great accuracy the patterns generated in horizontal oil-water flow, having exhibited a good agreement in the three-dimensional visualization of the phase arrangement in 5 of the 6 flow patterns studied. On the other hand, despite having included the same interfacial forces, the mixture model proved not to be as reliable in emulating the grade of dispersion in oil-in-water dispersed patterns.

The geometric reconstruction scheme allowed the tracking of interfaces in dispersed elements, facilitating the visualization of flow patterns similar to the captures in the experimental bench. However, the interface of the drops captured by this method depends on the volume fractions and the internal fluxes of cell clusters, so it cannot be ensured that the actual droplet size is outlined in the resulting pattern. Likewise, when simulating the dispersion of water in the oil (Dwo) flow pattern, it was not possible to observe water droplets covering the entire volume with any of the multiphase models, showing a considerable film of free oil. Thus, it is recommended to make new captures that allow identifying the experimental distribution of dispersed water droplets to compare with the model results and, therefore, achieve a better validation of its characterization in those flow conditions.

An adequate fit between the simulated and the experimental holdups was achieved, with an average relative error of 15.2%, while the results in the dispersed flow patterns showed pressure gradients very distant from those obtained experimentally, proving that the current model is not reliable to predict the pressure drop in all the flow patterns observed in horizontal oil-water flow.

The inclusion of radial interfacial forces as wall lubrication appears as a way to improve the accuracy of pressure drops calculated via CFD.

References

Abduvayt, P., Manabe, R., Watanabe, T., & Arihara, N. (2006). Analysis of oil/water-flow tests in horizontal, hilly terrain, and vertical pipes. *SPE Projects, Facilities and Construction*, *21*(1), 123–133. https://doi.org/10.2118/90096-ms

Al-Wahaibi, T., Smith, M., & Angeli, P. (2007). Transition between stratified and non-stratified horizontal oil–water flows. Part II: Mechanism of drop formation. *Chemical Engineering Science*, *62*(11), 2929–2940. https://doi.org/https://doi.org/10.1016/j.ces.2007.01.036

Al-Wahaibi, T., Yusuf, N., Al-Wahaibi, Y., & Al-Ajmi, A. (2012). Experimental study on the transition between stratified and non-stratified horizontal oil-water flow. *International Journal of Multiphase Flow*, *38*(1), 126–135. https://doi.org/10.1016/j.ijmultiphaseflow.2011.08.007

Al-yaari, M. A., & Abu-sharkh, B. F. (2011). CFD Prediction of Stratified Oil-Water Flow in a Horizontal Pipe. *Asian Transactions on Enigneering*, *01*(05), 68–75.

Amooey, A. A. (2016). Prediction of pressure drop for oil-water flow in horizontal pipes using an artificial neural network system. *Journal of Applied Fluid Mechanics*, *9*(5), 2469–2474. https://doi.org/10.18869/acadpub.jafm.68.236.24072

ANSYS Inc. (2021). *ANSYS®Academic Research Mechanical, Release 21.1, Help System*. ANSYS, Inc.

Azizi, S., Awad, M. M., & Ahmadloo, E. (2016). Prediction of water holdup in vertical and inclined oil–water two-phase flow using artificial neural network. *International Journal of Multiphase Flow*, *80*, 181–187. https://doi.org/https://doi.org/10.1016/j.ijmultiphaseflow.2015.12.010

Bochio, G., Cely, M. M. H., Teixeira, A. F. A., & Rodriguez, O. M. H. (2021). Experimental and numerical study of stratified viscous oil–water flow. *AIChE Journal*, *67*(6). https://doi.org/10.1002/aic.17239

Boostani, M., Karimi, H., & Azizi, S. (2017). Heat transfer to oil-water flow in horizontal and inclined pipes: Experimental investigation and ANN modeling. *International Journal of Thermal Sciences*, *111*, 340–350. https://doi.org/10.1016/j.ijthermalsci.2016.09.005

Brauner, N. (2001). The prediction of dispersed flows boundaries in liquid-liquid and gas-liquid systems. *International Journal of Multiphase Flow*, *27*(5), 885–910. https://doi.org/10.1016/S0301-9322(00)00056-2

Brauner, N. (2003). Liquid-Liquid Two-Phase Flow Systems. In V. Bertola (Ed.), *Modelling and Experimentation in Two-Phase Flow* (pp. 221–279). Springer Vienna. https://doi.org/10.1007/978-3-7091-2538-0_5

Burlutskiy, E., & Turangan, C. K. (2015). A computational fluid dynamics study on oil-in-water dispersion in vertical pipe flows. *Chemical Engineering Research and Design*, *93*(June), 48–54. https://doi.org/10.1016/j.cherd.2014.05.020

Cornejo Caceres, J. S., Prieto, N., Gonzalez, G., & Chaves-Guerrero, A. (2019). Numerical Simulation of a Natural Gas Cylindrical Cyclone Separator Using Computational Fluid Dynamics. *Industrial & Engineering Chemistry Research*, *58*(31), 14323–14332. https://doi.org/10.1021/acs.iecr.9b01217

Desamala, A. B., Dasmahapatra, A. K., & Mandal, T. K. (2014). Oil-Water Two-Phase Flow Characteristics in Horizontal Pipeline – A Comprehensive CFD Study. *International Journal of Chemical, Molecular, Nuclear, Materials and Metallurgical Engineering*, *8*(4), 371–375.

Flores, J. G., Chen, X. T., Sarica, C., & Brill, J. P. (1999). Characterization of oil-water flow

patterns in vertical and deviated wells. *SPE Production and Facilities*, *14*(2), 102–109. https://doi.org/10.2118/56108-pa

González Silva, G., Prieto, N., & Mercado, I. (2018). Large Eddy Simulation (LES) Aplicado a un lecho fluidizado gas – sólido. Parte I: Reactor a escala de laboratorio. *Revista UIS Ingenierías*, *17*(1), 93–104. https://doi.org/10.18273/revuin.v17n1-2018009

Grassi, B., Strazza, D., & Poesio, P. (2008). *International Journal of Multiphase Flow Experimental validation of theoretical models in two-phase high-viscosity ratio liquid – liquid flows in horizontal and slightly inclined pipes*. *34*, 950–965. https://doi.org/10.1016/j.ijmultiphaseflow.2008.03.006

Hamidi, M. J., Karimi, H., & Boostani, M. (2018). Flow patterns and heat transfer of oil-water two-phase upward flow in vertical pipe. *International Journal of Thermal Sciences*, *127*(November 2017), 173–180. https://doi.org/10.1016/j.ijthermalsci.2018.01.020

Hernández-Cely, M. M., & Ruiz-Diaz, C. M. (2020). Estudio de los fluidos aceite-agua a través del sensor basado en la permitividad eléctrica del patrón de fluido. *Revista UIS Ingenierías*, *19*(3), 177–186. https://doi.org/10.18273/revuin.v19n3-2020017

Kang, Q., Gu, J., Qi, X., Wu, T., Wang, S., Chen, S., Wang, W., & Gong, J. (2021). Hydrodynamic modeling of oil–water stratified smooth two-phase turbulent flow in horizontal circular pipes. *Energies*, *14*(16), 1–18. https://doi.org/10.3390/en14165201

Parvini, M., Dabir, B., & Mohtashami, S. A. (2010). Numerical Simulation of Oil Dispersions in Vertical Pipe Flow. *Journal of the Japan Petroleum Institute*, *53*(1), 42–54. https://doi.org/10.1627/jpi.53.42

Pouraria, H., Kwan, J., & Kee, J. (2016). Numerical modelling of two-phase oil – water fl ow patterns in a subsea pipeline. *Ocean Engineering*, *115*, 135–148.

https://doi.org/10.1016/j.oceaneng.2016.02.007

Rodriguez, O. M. H., & Baldani, L. S. (2012). Journal of Petroleum Science and Engineering Prediction of pressure gradient and holdup in wavy stratified liquid – liquid inclined pipe flow. *Journal of Petroleum Science and Engineering*, *96–97*, 140–151. https://doi.org/10.1016/j.petrol.2012.09.007

Rodriguez, O. M. H., Rodriguez, I. H., & Ansoni, J. L. (2019). An experimental and numerical study on the wall lubrication force in dispersed liquid-liquid flow. *International Journal of Multiphase Flow*, *120*, 103094. https://doi.org/https://doi.org/10.1016/j.ijmultiphaseflow.2019.103094

Rudman, M. (1997). Volume-tracking methods for interfacial flow calculations. *International Journal for Numerical Methods in Fluids*, *24*(7), 671–691. https://doi.org/10.1002/(SICI)1097-0363(19970415)24:7<671::AID-FLD508>3.0.CO;2-9

Ruiz-Diaz, C. M., Gómez-Camperos, J. A., & Hernández-Cely, M. M. (2022). Flow pattern identification of liquid-liquid (oil and water) in vertical pipelines using machine learning techniques. *Journal of Physics: Conference Series*, *2163*(1), 12001. https://doi.org/10.1088/1742-6596/2163/1/012001

Ruiz-Diaz, C. M., Hernández-Cely, M. M., & González-Estrada, O. A. (2021a). Modelo predictivo para la identificación de la fracción volumétrica en flujo bifásico. *Ciencia En Desarrollo*, *12*(2), 49–55. https://doi.org/10.19053/01217488.v12.n2.2021.13417

Ruiz-Diaz, C. M., Hernández-Cely, M. M., & González-Estrada, O. A. (2021b). Analysis of liquid-liquid (water and oil) two-phase flow in vertical pipes, applying artificial intelligence techniques. *Journal of Physics: Conference Series*, *2046*(1), 012016. https://doi.org/10.1088/1742-6596/2046/1/012016

Rusche, H., & Issa, R. I. (2000). The effect of voidage on the drag force on particles, droplets and bubbles in dispersed two-phase flow. In G. Matsui, I. Žun, & G. P. Celata (Eds.), *Japanese-European Two-Phase Flow Meeting*.

Shi, J., Gourma, M., & Yeung, H. (2017). CFD simulation of horizontal oil-water flow with matched density and medium viscosity ratio in different flow regimes. *Journal of Petroleum Science and Engineering*, *151*(December 2016), 373–383. https://doi.org/10.1016/j.petrol.2017.01.022

Shi, J., Gourma, M., & Yeung, H. (2021). A CFD study on horizontal oil-water flow with high viscosity ratio. *Chemical Engineering Science*, *229*, 116097. https://doi.org/10.1016/j.ces.2020.116097

Shih, T.-H., Liou, W. W., Shabbir, A., Yang, Z., & Zhu, J. (1995). A new k-ϵ eddy viscosity model for high reynolds number turbulent flows. *Computers & Fluids*, *24*(3), 227–238. https://doi.org/https://doi.org/10.1016/0045-7930(94)00032-T

Sridhar, S., Zhang, H. Q., Sarica, C., & Pereyra, E. (2011). Experiments and model assessment on high-viscosity oil/water inclined pipe flows. *Proceedings - SPE Annual Technical Conference and Exhibition*, *2*, 1554–1563. https://doi.org/10.2118/146448-ms

Trallero, J. L., Sarica, C., & Brill, J. P. (1997). A study of oil/water flow patterns in horizontal pipes. *SPE Production and Facilities*, *12*(3), 165–172. https://doi.org/10.2118/36609-PA

Walvekar, R. G. (2010). Effect of Interphase Forces on Two-Phase Liquid-Liquid Flow in Horizontal Pipe. *Institute of Engineers Malaysia*, *71*(2), 35–40.

Walvekar, R. G., Choong, T. S. Y., Hussain, S. A., Khalid, M., & Chuah, T. G. (2009). Numerical study of dispersed oil–water turbulent flow in horizontal tube. *Journal of Petroleum Science and Engineering*, *65*(3), 123–128.

https://doi.org/https://doi.org/10.1016/j.petrol.2008.12.019

Wu, Y., Guo, H., Song, H., & Deng, R. (2022). Fuzzy inference system application for oil-water flow patterns identification. *Energy*, *239*, 122359. https://doi.org/10.1016/j.energy.2021.122359

Yadigaroglu, G., & Hewitt, G. F. (2018). Introduction to Multiphase Flow. In G. Yadigaroglu & G. F. Hewitt (Eds.), *Zurich Lectures on Multiphase Flow* (1st ed.). Springer Cham. https://doi.org/10.1007/978-3-319-58718-9

Appendices

Appendix A. Ansys Workbench configuration

The model implemented in Ansys Workbench uses three sections to simulate the two-phase oil-water flow. The geometry section was developed in SpaceClaim, the meshing method was programmed in ICEM CFD, and the flow dynamics simulation was developed in Ansys Fluent. Figure A1 shows the relationship between the modules that make up the program.

Figure A1

Network of modules implemented in Ansys Workbench

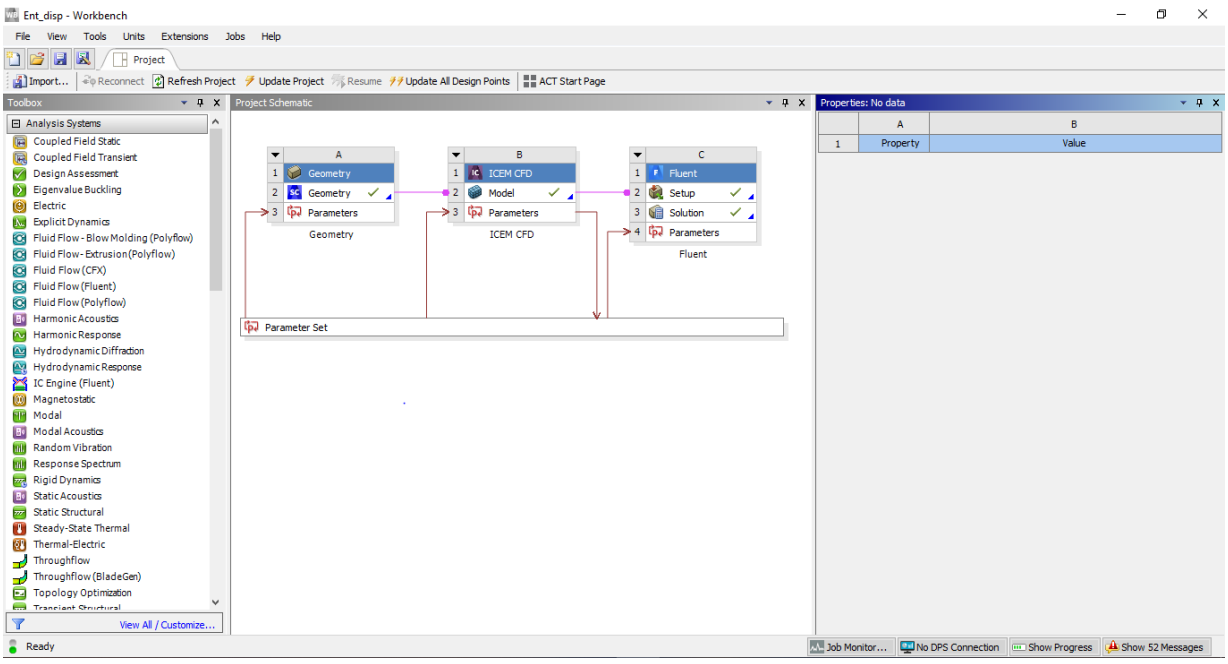

The ability to parameterize most of the variables specified in these three modules, for their subsequent manipulation from the Ansys Workbench interface, facilitates the automation of

processes in this software. Figure A2 shows the Parameter Set tab, available by double-clicking on the box of the same name in the main window, where all the parameters used in the program are found.

Figure A2

Parameter Set window

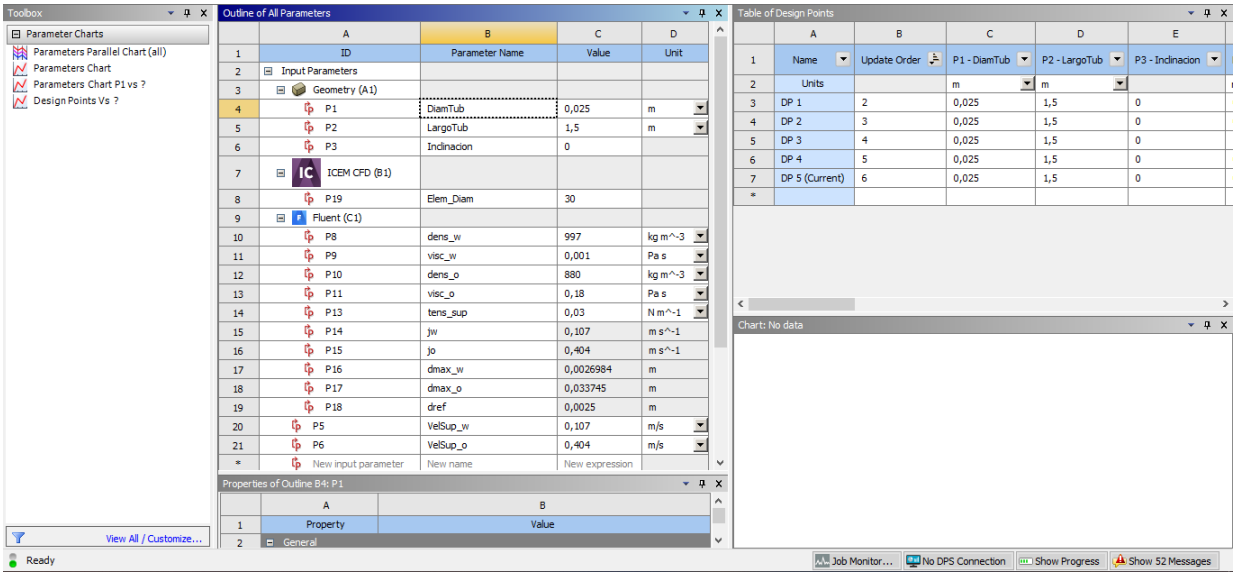

Regarding the geometry of the model, since it is a straight pipe with a homogeneous section, it is only necessary to insert the desired magnitudes of diameter and length. Similarly, even though there is also the option of working with inclinations other than 0°, it is recommended to take more precautions to model inclined or vertical pipes, as the implemented mathematical models have not been tested under those flow conditions. The generation of work mesh only depends on the parameter *Elem_Diam* that represents the number of elements that fit in the diameter of the pipe, thus its value affects the element size and hence serves as a quantification of the mesh refinement. The process by which the program allows the configuration of different

meshes to simulate the two-phase flow in pipes of various dimensions is explained more deeply in Appendix B.

The input parameters required for the flow dynamics simulation in Ansys Fluent are the superficial velocities (J_w and J_o) and the relevant properties of the working fluids, including the density and viscosity of water and oil and the interfacial tension between both fluids. Regarding the properties of water, unless the operating temperature is very distant from the standard state temperature, they do not tend to require any modification, likewise, the interfacial tension between water and oil is a property that can be assumed with the value of 0.03 N/m if mineral oil is used and there are no experimental records of this property. The configuration required in Fluent to simulate the flow dynamics from these parameters is explained in Appendix C.

Appendix B. Geometry and meshing configuration

To modify the dimensions of the pipe, the respective parameters can be accessed through the *Parameter Set* tab shown in Figure A2. It is worth clarifying that the relationship between pipe length and diameter should be high enough to develop the flow pattern to be analyzed. Based on the tests carried out, a $(L/D)_{Tub}$ ratio greater than or equal to 50 is recommended to ensure correct development and visualization of the pattern.

When modifying the dimensions of the pipe, the *Geometry* module must be refreshed, as shown in Figure B1, and then the Workbench project must be saved so that the updated geometry is available for meshing in ICEM.

Figure B1

Refreshing of the geometry after updating parameters

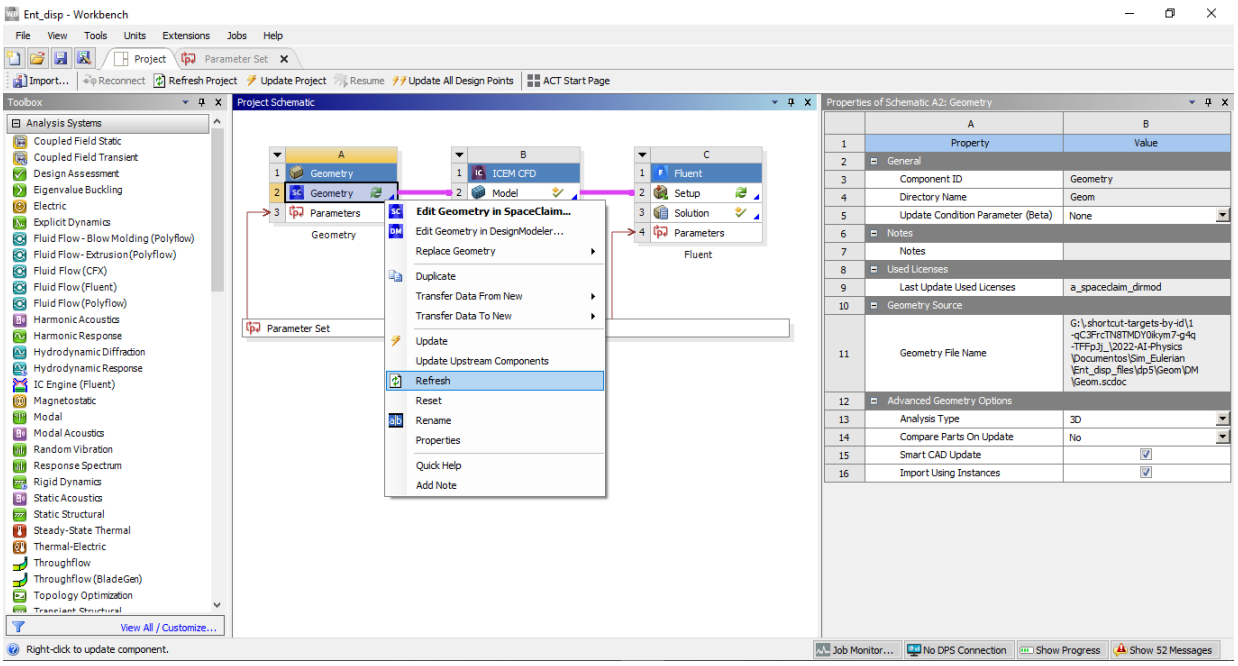

The update of the geometry not only generates a pipe with the desired dimensions, but also the *Named Selections* required for the definition of the boundary conditions, these being *Inlet*, *Wall*, and *Outlet.*

Finally, to generate the structured mesh, ICEM CFD can incorporate a code in Tcl/tk language, shown in Appendix D, through which the meshing process is automated to generate high-quality O-H meshes by specifying only the parameter *Elem_Diam* in the *Set Parameter* tab to define the degree of refinement that is desired. The recommended value of this parameter is 30 since the independence test showed good results with this degree of refinement; however, it is possible to work with more refined meshes by increasing the number of elements per diameter.

As the internal process of meshing is included in the incorporated code, to generate a new mesh, whether with different geometry or refinement, the code must be executed by selecting *Update* in the ICEM module, as shown in Figure B2.

Figure B2

Update of the ICEM CFD module

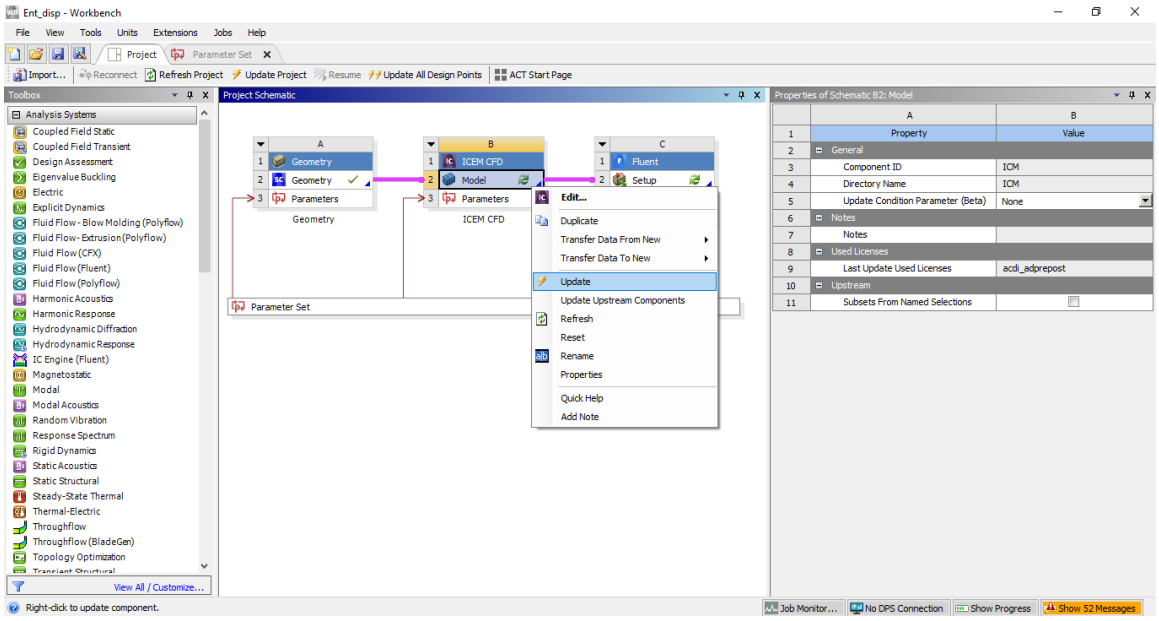

Appendix C. Ansys Fluent configuration

Once the parameters required in this module have been defined, Fluent is entered through the *Setup* box of the corresponding module, which generates the pop-up window shown in Figure C1, which warns that in this way the data processed in previous simulations cannot be accessed, but rather new Fluent settings can be updated, including the mesh and parameter values.

Figure C1

Warning pop-up window when Fluent is accessed through Setup

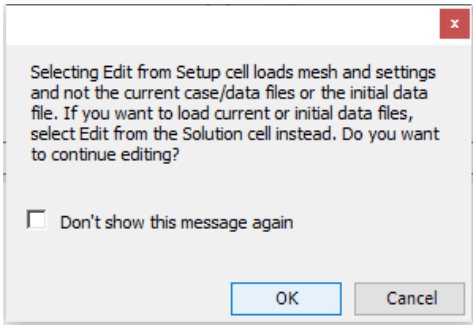

In addition to this pop-up window, Figure C2 shows other windows that can appear in case of detecting changes in the mesh or the flow parameters. In any case, in all these pop-up windows it is enough to answer them affirmatively to start loading Fluent.

Figure C2

Appearing pop-up windows when reported changes in mesh or parameter values

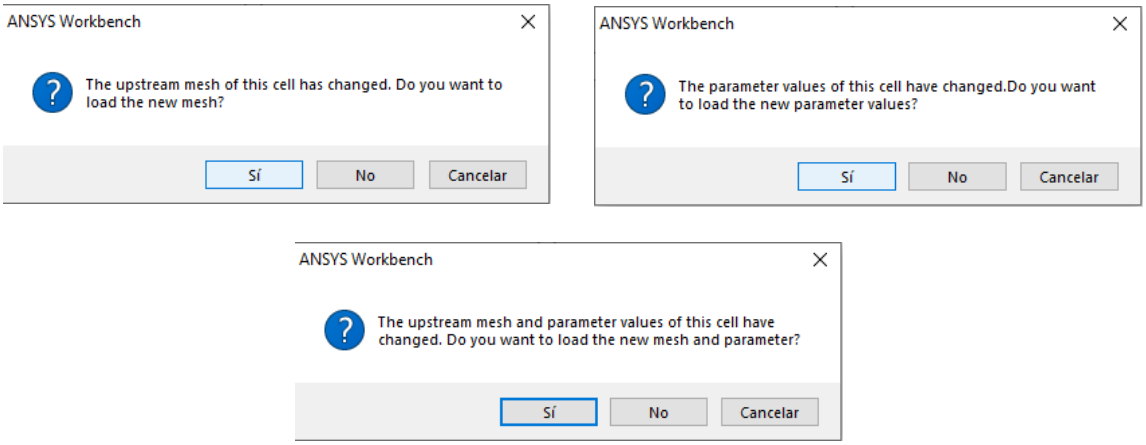

Next, in the *Fluent Launcher* window, the *Double Precision* box must be checked for the calculation of multiphase systems such as the one presented in this work, and Fluent can start.

Figure C3

Fluent Launcher window

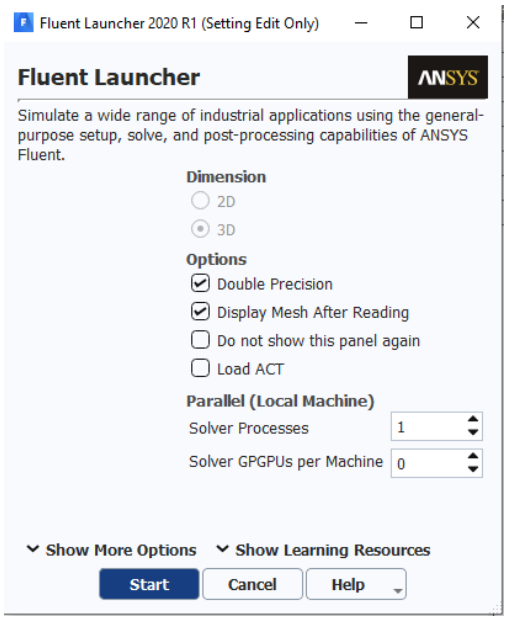

When entering Fluent, the first thing to do is configure the multiphase model, by accessing the *Multiphase Models* window as shown in Figure C4.

Figure C4

Ways of accessing the window Multiphase Model in Fluent

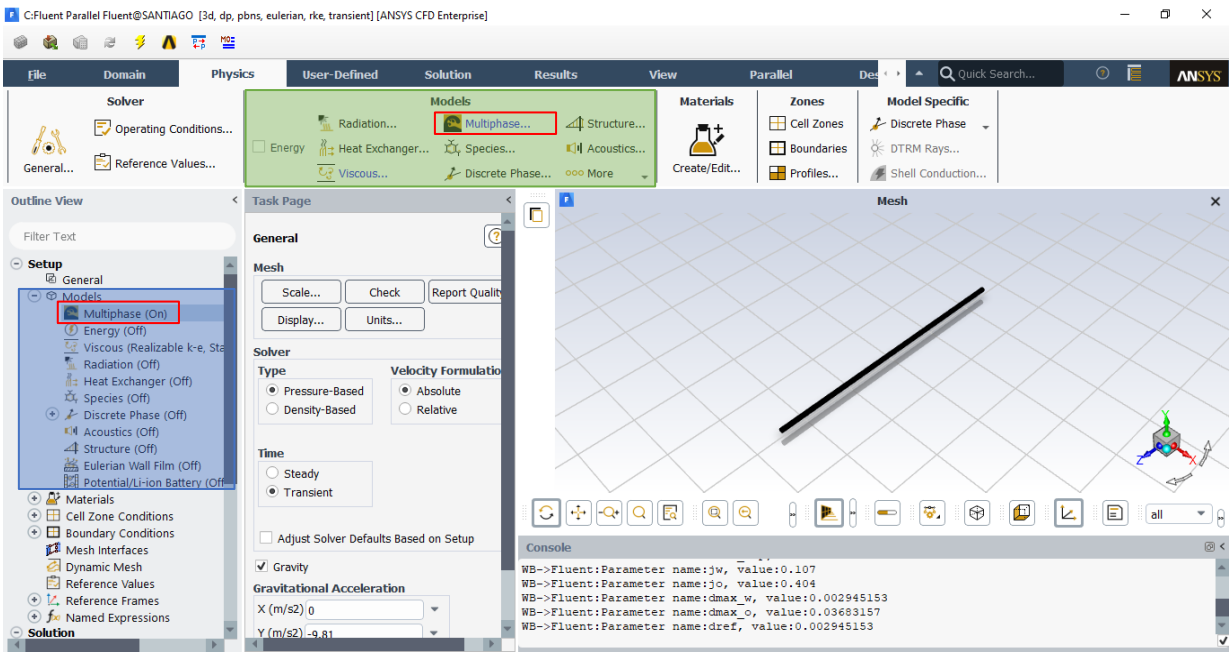

In the appearing window, the *Phases* tab allows the selection of the primary and secondary fluid in the *Phase Material* drop-down menu, choosing the fluid with the highest superficial velocity for the primary fluid. Figure C5 shows the characteristics that can be modified in the *Phases* tab, among which the droplet diameter stands out in the secondary phase configuration.

Figure C5

Phases selection for the multiphase model

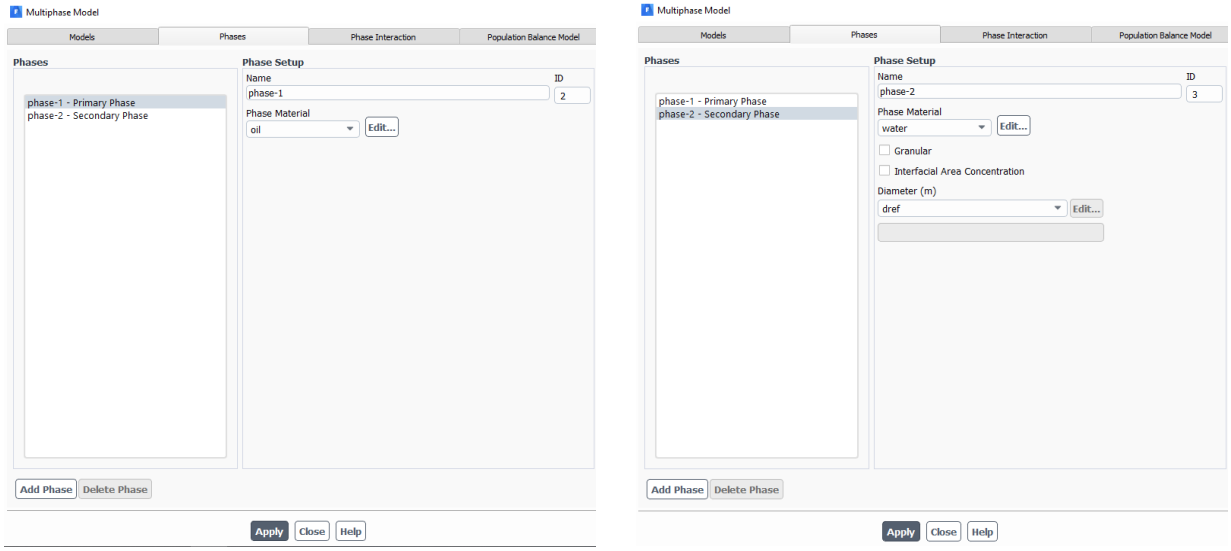

The droplet diameter used in the program is determined from a Workbench parameter called *dref*, which in turn depends on the parameters *dmax_o* and *dmax_w*, also present in the *Parameter Set* of Figure A2. These last parameters represent the maximum oil droplet diameter and maximum water droplet diameter, expressed based on the Brauner model by modifying the continuous and dispersed fluid to differentiate both cases.

$$d_{\max\_o} = 7.61D\left(\frac{\rho_w D}{\mu_w \sigma}\right)^{-0.52}\left(\frac{\sigma^{0.08}}{\mu_w^{0.6}}\right)\left(\frac{J_o}{J_w * (J_w + J_o)^{1.12}}\right)\left(1 + \frac{\rho_o J_o}{\rho_w J_w}\right)^{-0.4} \tag{38}$$

$$d_{\max\_w} = 7.61D\left(\frac{\rho_o D}{\mu_o \sigma}\right)^{-0.52}\left(\frac{\sigma^{0.08}}{\mu_o^{0.6}}\right)\left(\frac{J_w}{J_o * (J_w + J_o)^{1.12}}\right)\left(1 + \frac{\rho_w J_w}{\rho_o J_o}\right)^{-0.4} \tag{39}$$

$$d_{ref} = \min\left(\left(d_{\max\_o} * F\right) + \left(d_{\max\_w} * (1 - F)\right), \frac{D}{10}\right) \tag{40}$$

The variable F, used in Equation (40), defines which fluid is assumed to be dispersed, taking a value of 0 if water is the dispersed fluid and a value of 1 otherwise. For the model used in

the program, considering that the fluid with the highest superficial velocity is the continuous one, the variable F may be calculated with the following equation.

$$F = \text{round}\left(\tanh\left(0.549306 * \frac{J_w}{J_o}\right)\right) \tag{41}$$

Unlike the expressions used to define the droplet diameter, Fluent allows defining of some parameters through expressions, such as those used in boundary conditions.

To configure the boundary conditions, it is necessary to enter the *Boundary Conditions* section as shown in Figure C6, and link the *Named Selections* with their respective boundary condition in the *Type* drop-down menu.

Figure C6

Ways of accessing the Boundary Conditions setup

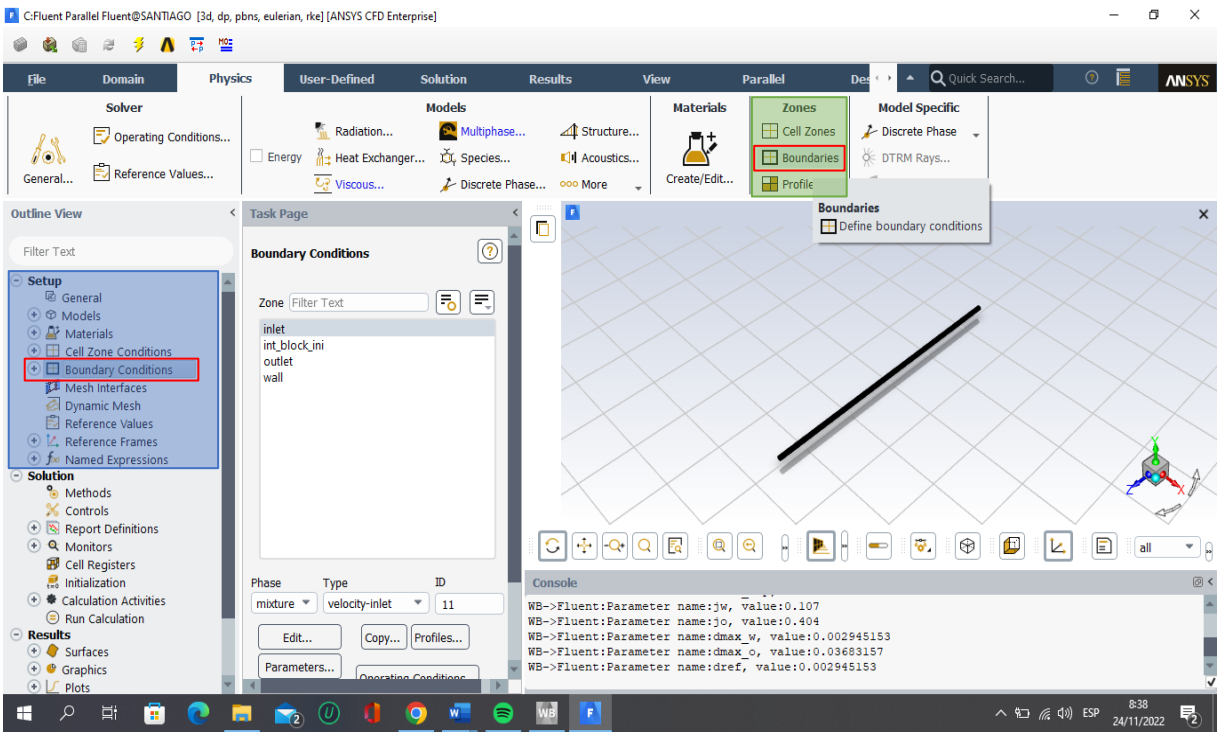

While the definition of wall and outlet boundary conditions is complete by simply linking their respective named selections to the *wall* and *pressure-outlet* types in the drop-down menu, as shown in Figure C7, with the *velocity-inlet* condition, applied to the *Inlet* surface, some variables must be defined, such as the flow velocity, turbulent intensity, and volume fraction in the section.

Figure C7

Selection of the corresponding boundary condition for each zone

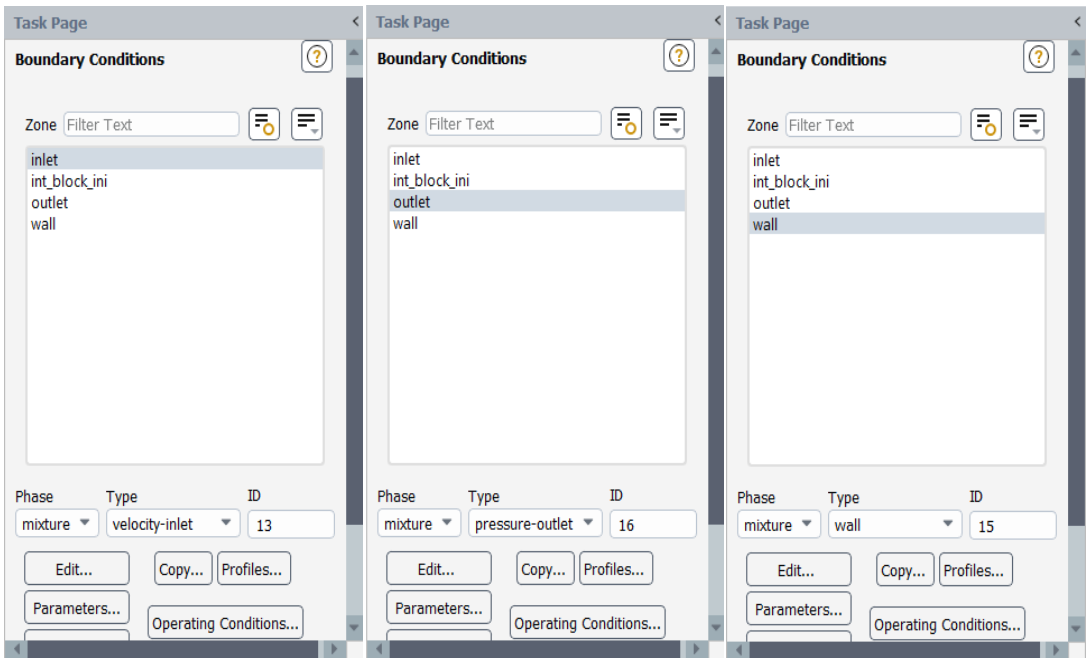

By changing the selected option in the *Phase* drop-down menu, different characteristics of the input boundary condition can be edited, as shown in Figure C8.

Figure C8

Setup of the Inlet boundary condition

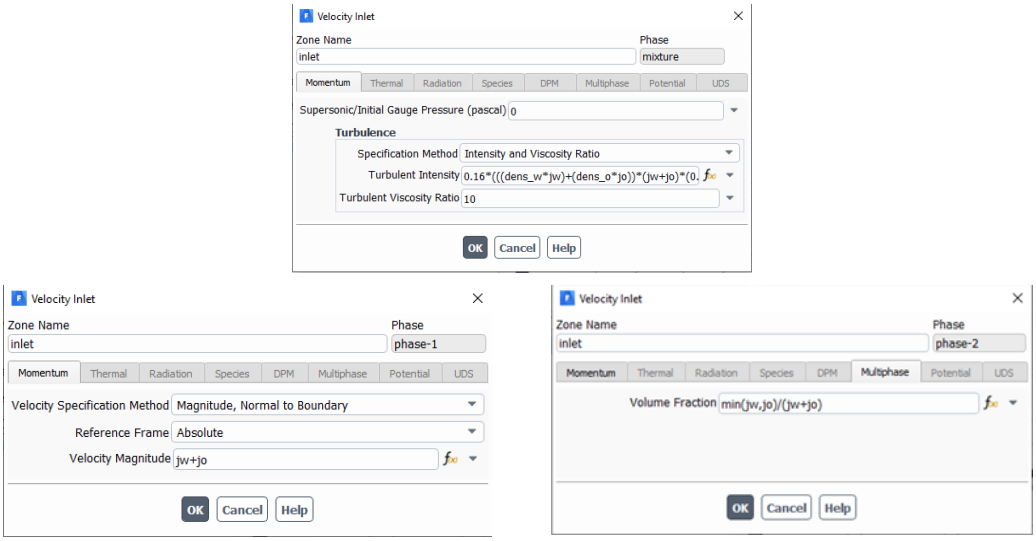

From the Fluent expressions shown previously, it can be noted that the magnitude of the velocity of each phase agrees with Equation (35), while the expression for turbulent intensity uses the expanded form developed in Equation (42). Regarding the volume fraction, since it is defined only in the secondary phase, and this phase corresponds to the one with the lowest superficial velocity, Equation (43) can be used.

$$I_t = 0.16Re^{-1/8} = 0.16\left(\frac{(\rho_w J_w + \rho_o J_o)(J_w + J_o)D}{\mu_w J_w + \mu_o J_o}\right)^{-1/8} \tag{42}$$

$$\alpha_{phase-2} = \frac{\min(J_w, J_o)}{J_w + J_o} \tag{43}$$

While the previously mentioned procedure only covers the definition of the phases and boundary conditions, the configuration required to optimally simulate any type of biphasic water-

oil flow consists of a three-stage process: Steady-state simulation, transient simulation, and geometric reconstruction

1. Steady-state simulation

Steady-state simulation is used to get a proper starting point for transient simulation. This type of modeling can be very accurate in several cases, but it is not recommended when the studies are highly dependent on the initial conditions, so it is not taken as the final processing in this model.

To configure the simulation in a steady state, the *General* setup is accessed as shown in Figure C9, and the *Steady* option is selected in *Time* panel. Another aspect to consider in this section is the inclusion of gravity in the model, applying the value of -9.81 in the *y* component.

Figure C9

General setup

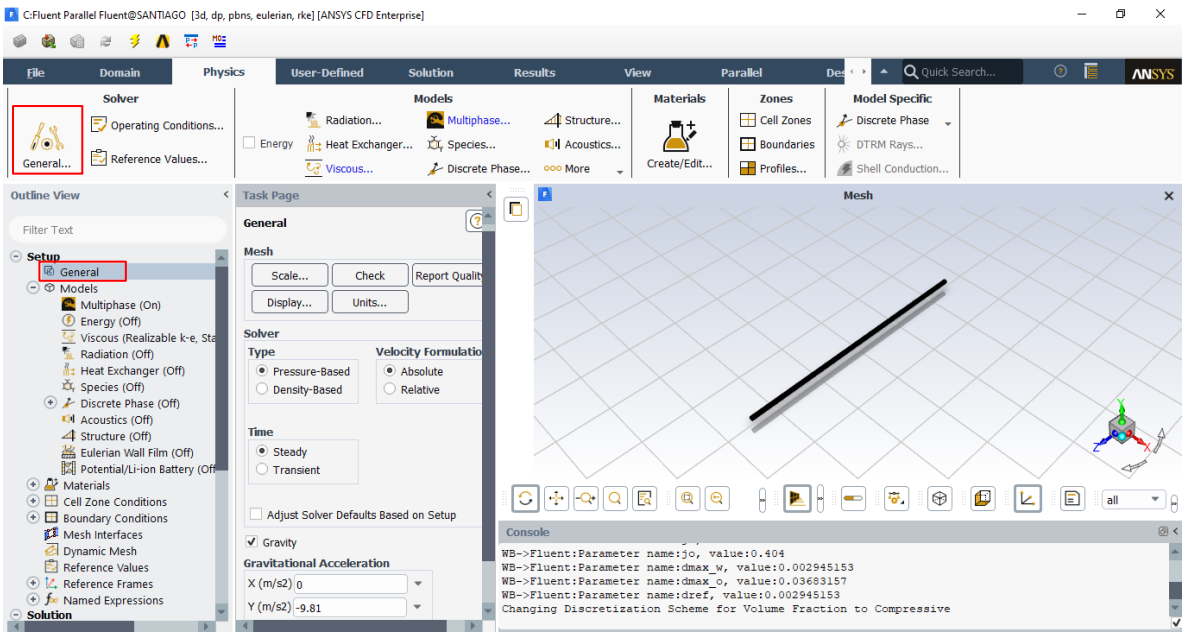

When entering the *Multiphase Model* window in the *Models* tab, shown in Figure C10, it is possible to choose the mixture and Eulerian-Eulerian multiphase models, as well as the model formulation, using the *Implicit* formulation for this simulation stage.

Figure C10

Configuration of the multiphase model for steady-state simulation

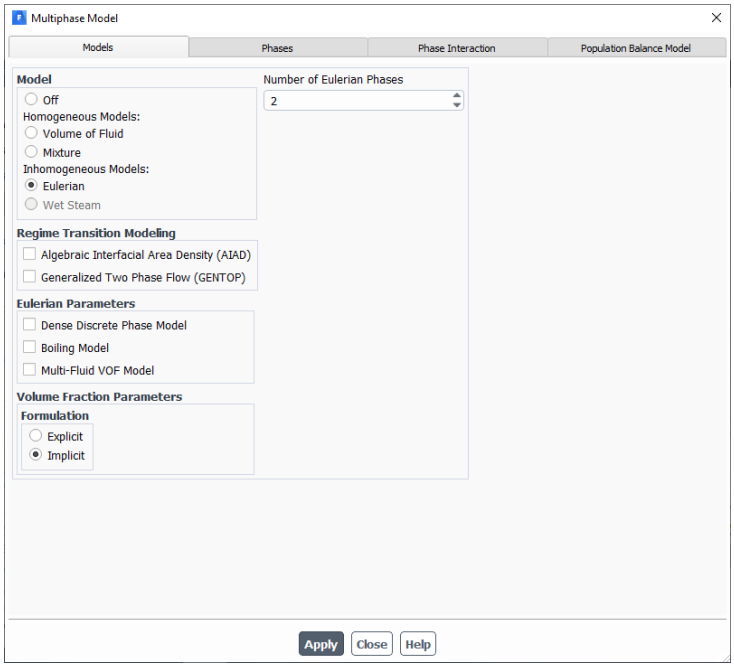

Figure C11 shows the two sections of the *Phase Interaction* tab that are relevant to this model. In the *Forces* section, it is observed that the only interaction forces included in this model are the surface tension and the drag force. Although the modeling of the surface tension through the *Continuum Surface Force (CSF)* scheme is not strictly required for this stage of the simulation, the modeling of the drag force with the *Symmetric* model has shown to be the only one that allows obtaining good approximations to the expected results. On the other hand, the *Interfacial Area*

section only allows the selection of the interfacial area concentration model, which is kept in *Symmetric* for the entire simulation.

Figure C11

Configuration of the Phase Interaction models for steady-state simulation

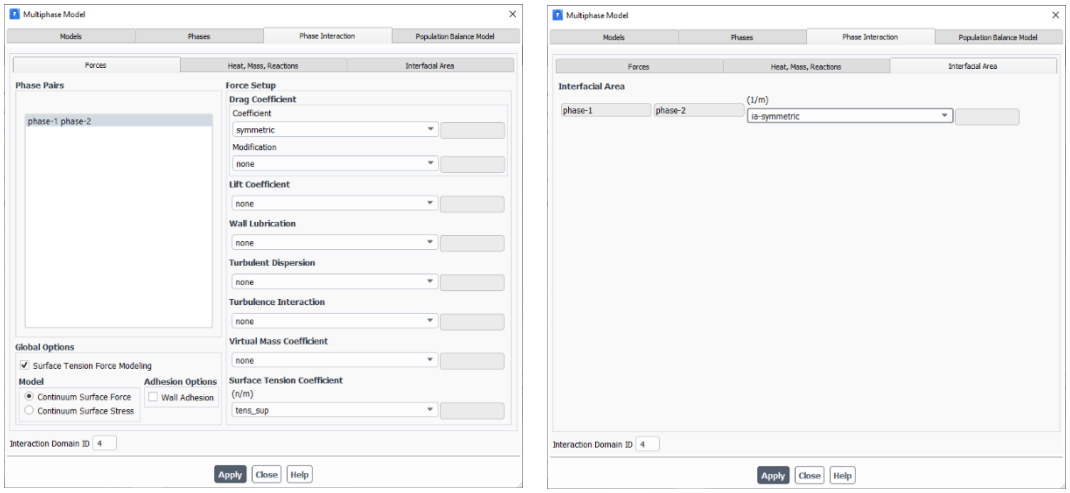

Then, to define the Realizable *k-ε* turbulence model, used throughout the simulation, the *Viscous Model* window is accessed as shown in Figure C12, and there the *k-epsilon* option is selected in the panel *Model* and the type *Realizable* in the panel below.

With the turbulence model defined, *Methods* option is selected in the *Solution* tab to configure the resolution algorithms of the implemented models. In the resulting section, the *Phase Coupled SIMPLE* scheme is selected for the pressure-velocity coupling (*SIMPLE* when mixture multiphase model is used) and the *PRESTO!* algorithm for pressure discretization, keeping *First Order Upwind* selected in the other discretization menus, as shown in Figure C13.

Figure C12

Setup of the turbulence model

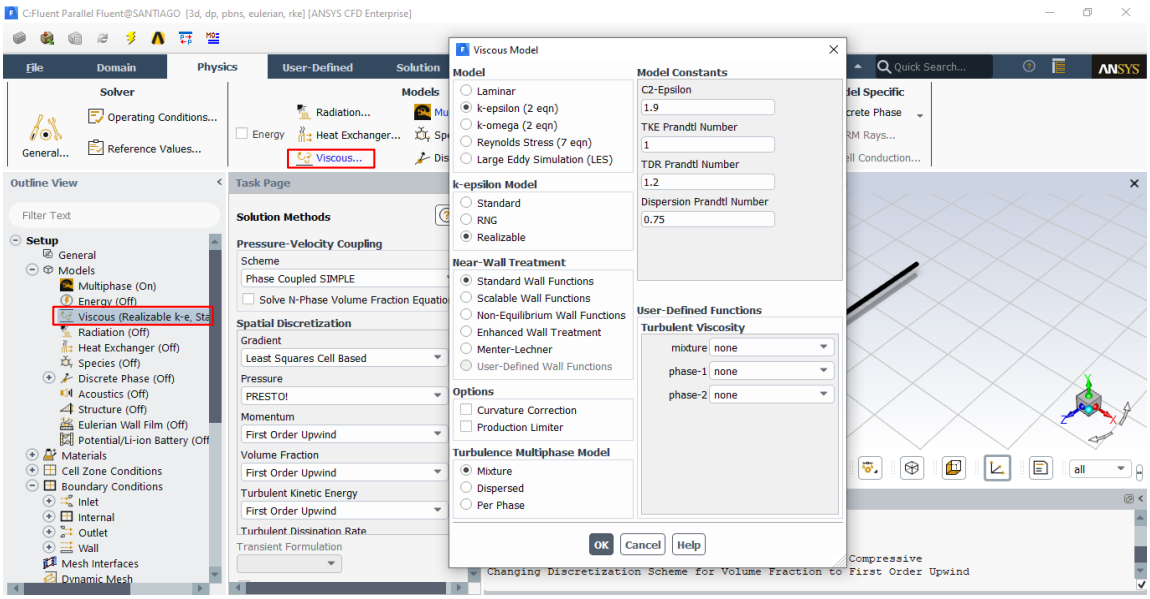

Figure C13

Access and configuration of the Solution Methods

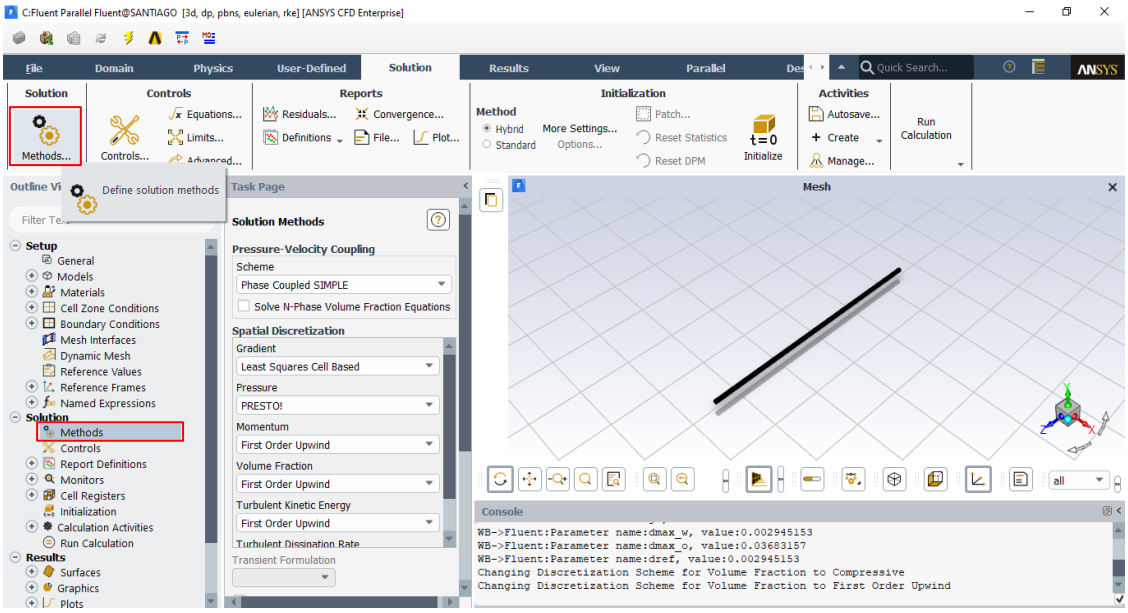

For this stage, a hybrid initialization of the flow parameters is performed by selecting *Hybrid Initialization* in the *Solution initialization* section seen in Figure C14.

Figure C14

Initialization of the steady-state simulation

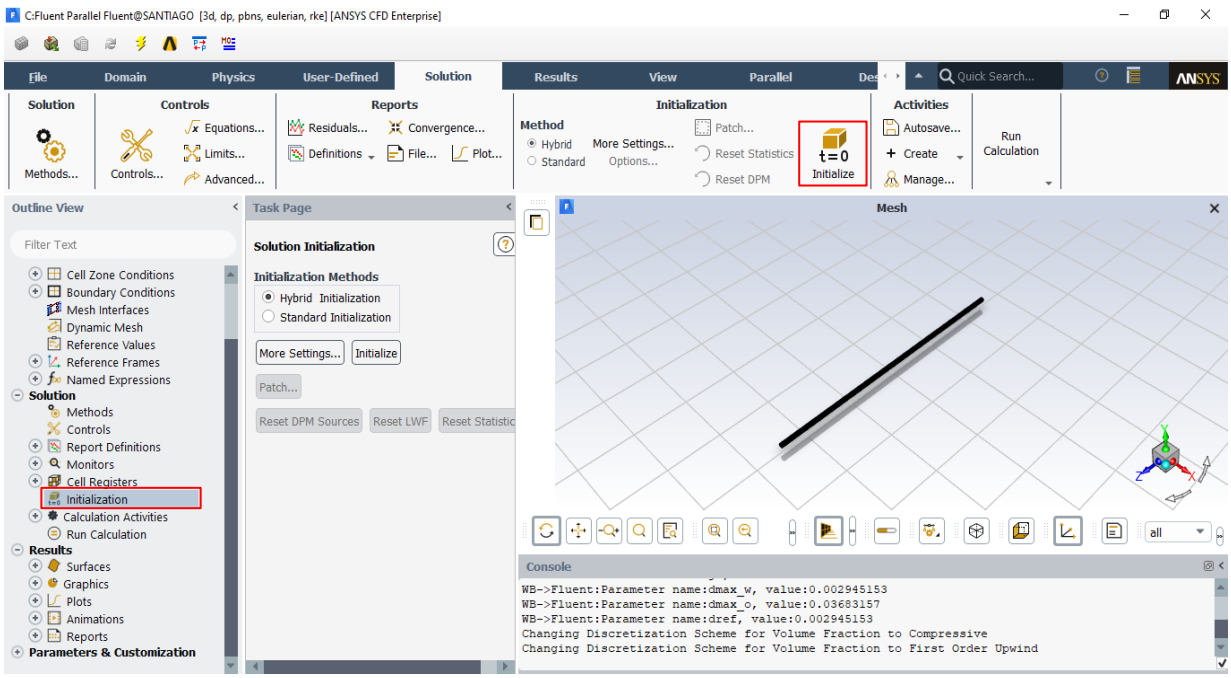

At the end of the initialization, the simulation is configured to perform 500 iterations in the *Run Calculation* section shown in Figure C15, and the simulation is executed, concluding this stage.

Figure C15

Setup of the iterations used in the steady-state simulation

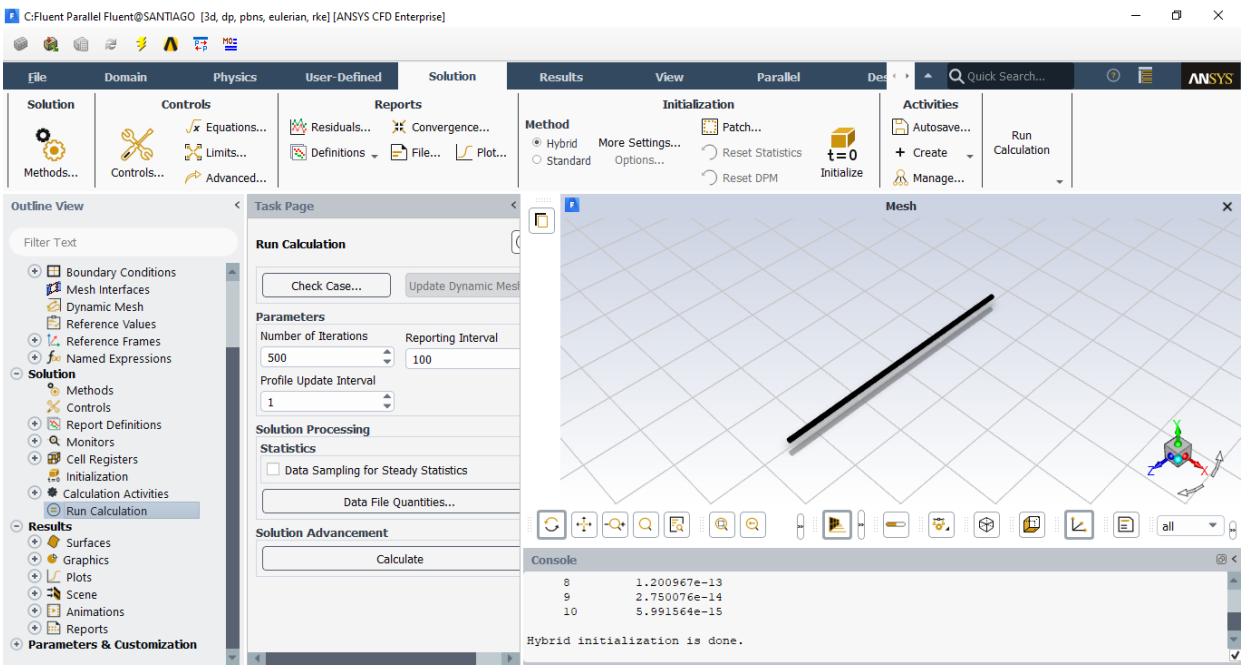

2. Transient simulation

To start with this stage, in the *Models* tab of the *Multiphase Model* window, the *Explicit* option is selected, and the changes are applied. This change not only enables new settings, as seen in Figure C16, but also automatically changes the simulation mode from steady state to transient.

Likewise, in the *Phase Interaction* tab, the drag model must be modified to the Rusche-Issa model, which is added to the program as a UDF, so in the drop-down menu corresponding to *Drag Coefficient* the option *user-defined* is selected to show a new pop-up window where the only UDF available in the program is chosen, as shown in Figure C17.

Figure C16

Modification of the multiphase model configuration for transient simulation

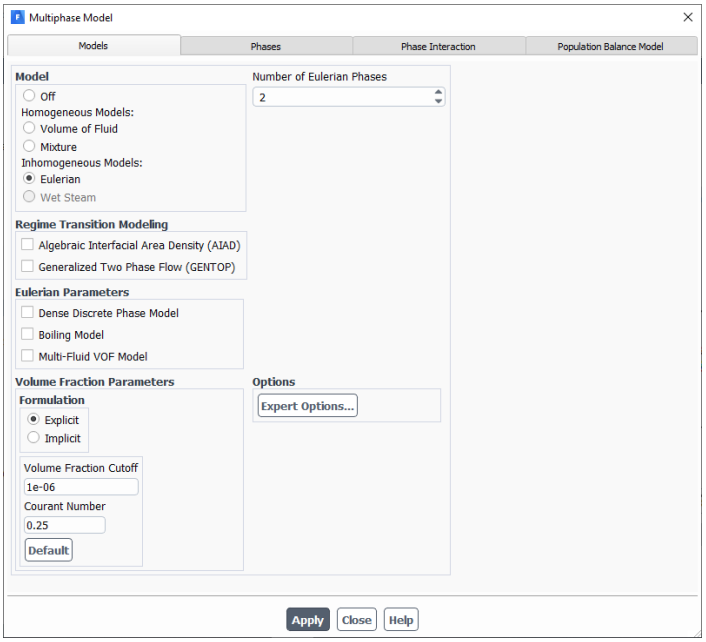

Figure C17

Selection of the Rusche-Issa drag model in Fluent

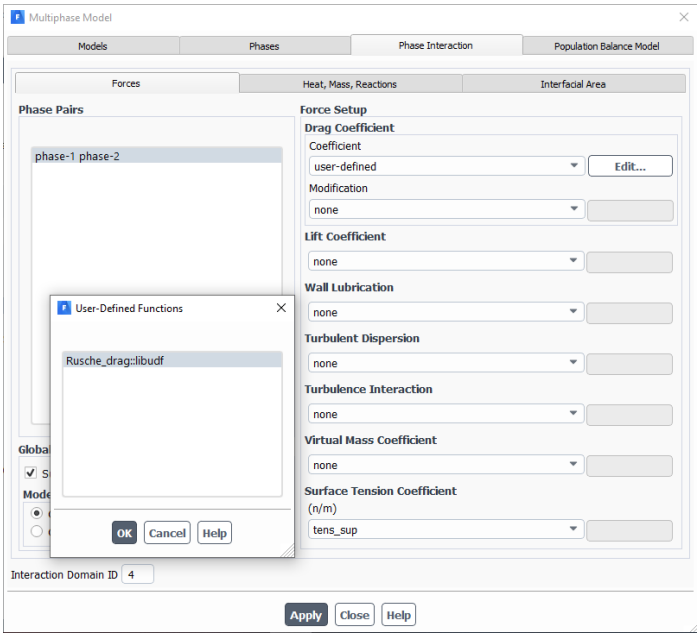

When applying the changes in the multiphase model, the subsequent modification is applied to the resolution algorithms present in the *Solution methods* section, specifically the spatial discretization of the flow parameters, instead of using the *First Order Upwind* scheme as in the previous stage, the *QUICK* scheme is selected, which allows obtaining more precise results as it is a second-order method. Figure C18 shows the changes made in this process.

Figure C18

Setup of the Solution Methods section in transient simulation

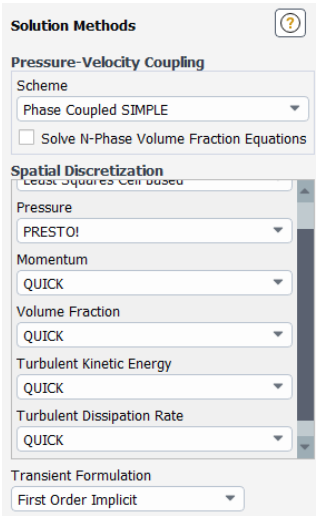

Since the flow parameters in this simulation are already initialized with the values obtained from the first stage, the process continues directly with the simulation execution, accessing the *Run Calculation* section to configure the time parameters required in the process. Figure C19 shows the configuration used, in which the *Adaptive* type is used to adjust the advance of time since this handles the greatest advance of the time that meets a certain condition of the global Courant number. This number represents the relationship between the magnitude of each time step

and the time required for the flow to pass through any cell, with 4 being the maximum value recommended by Fluent to avoid convergence problems.

Figure C19

Setup of the Run Calculation section in transient simulation

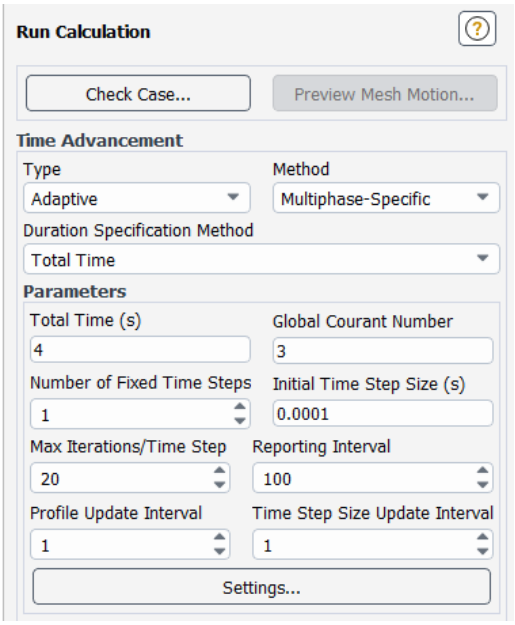

In the previous figure, it can also be noted that to configure the duration specification, the *Total Time* method is chosen, specifying the total flow time which, considering that it must be high enough to guarantee the stability of the transient system, can be approximated as the flow residence time, expressed by the following equation.

$$t_{Total} \approx \frac{L_{Tub}}{J_w + J_o} \tag{44}$$

Finally, after setting the value of the global Courant number and the initial time step, the transient simulation can start.

3. Geometric Reconstruction

The results of the transient simulation are appropriate to analyze the model accuracy to predict different flow parameters, such as pressure, velocity, and phase distribution, however, the mixture and Eulerian-Eulerian multiphase models discretize the volume fraction with a dispersed interface, so there is no tendency to form closed volumes for the expected drops.

The main alternative to address this problem and achieve a realistic three-dimensional visualization of flow patterns is the use of geometric reconstruction algorithms. Geometric reconstruction in Fluent is only available in the VOF multiphase model, with which interfaces of low complexity, like those observed in separate flows, can be accurately differentiated.

To apply the geometric reconstruction in the other multiphase models, access the *Multiphase Models* window in the *Models* tab and select the *Multi-fluid VOF Model* box. When activating this box, a new selection panel called “Interface Modeling” appears, where the *Sharp* option is selected, as shown in Figure C20, to enable the geometric reconstruction scheme.

The inclusion of the geometric reconstruction is realized in the *Solution Methods* section, selecting the *Geo-Reconstruct* option in the drop-down menu corresponding to the volume fraction discretization, as shown in Figure C21.

Figure C20

Configuration of the multiphase model to enable geometric reconstruction

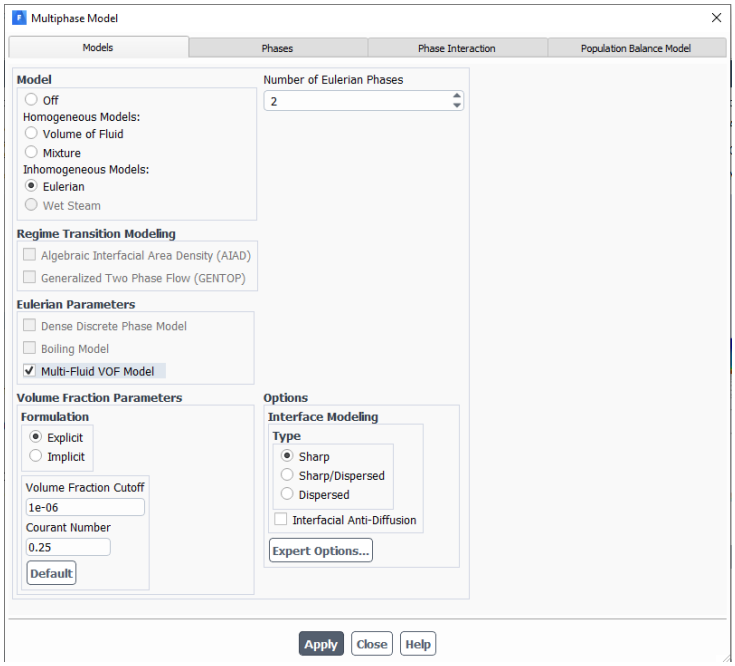

Figure C21

Selection of the geometric reconstruction scheme in the Solution Methods section

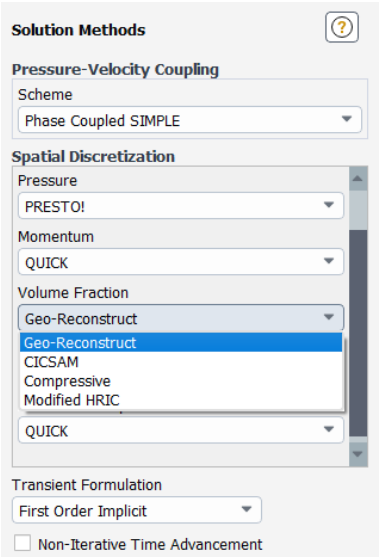

The inclusion of the geometric reconstruction equations in the model implies a greater difficulty in achieving convergence, which is why in the *Run Calculation* section, shown in Figure C22, the number of iterations required for each step is increased to 30. Likewise, the slow convergence makes it preferable to apply a few time steps in this stage, even more considering that the flow parameters are already developed.

Figure C22

Setup of the last simulation parameters to apply the geometric reconstruction

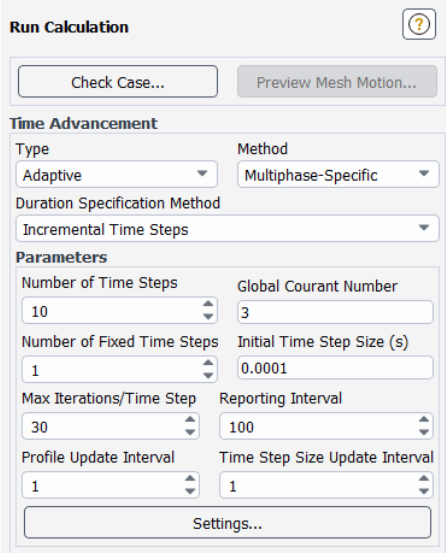

The duration specification method is changed to *Incremental Time Steps* to specify the number of additional time steps to be calculated in this stage, and the simulation can start.

After the last simulation ends, an *Iso-Surface* is created as shown in Figure C23, setting the value of 0.3 for the volume fraction of the primary phase as a reference, to capture the transition between phases. This iso-surface is what makes it possible to visualize the interface in a three-dimensional way, but also, to more clearly differentiate the volume occupied by the phases an *Iso-*

Clip surface is created for each phase according to the volume fractions, with which the wall surface gets divided into the area occupied by the primary fluid and that occupied by the secondary.

Figure C23

Creation of the iso-surface representing the interface

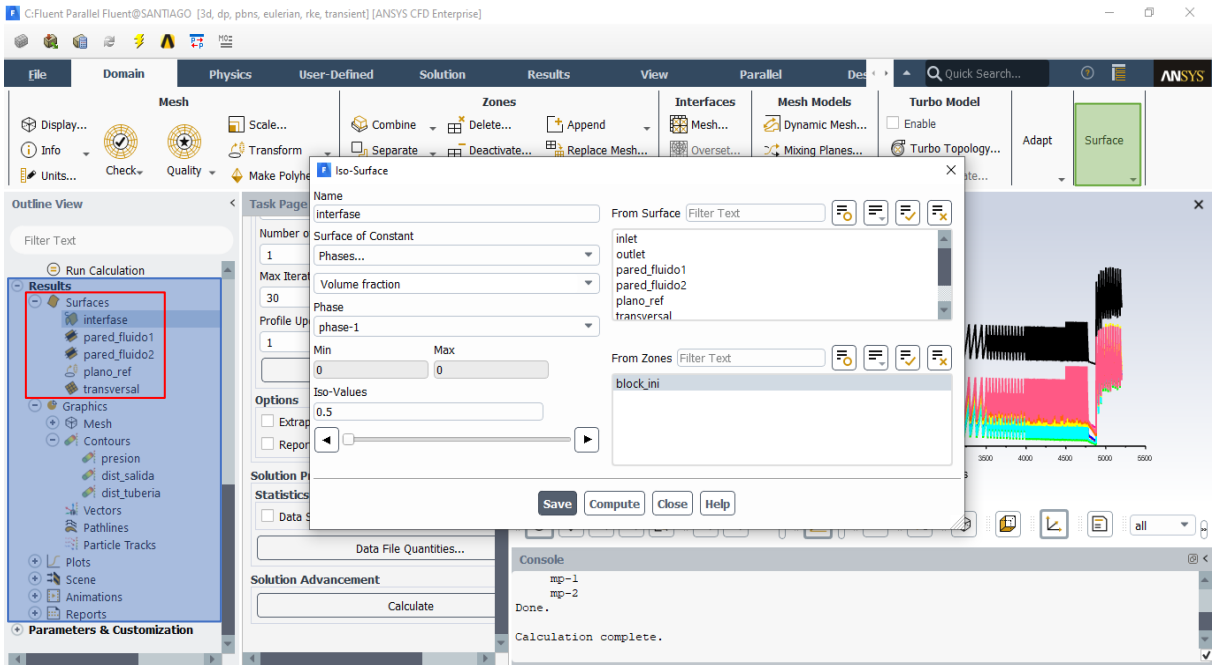

Figure C24 shows the setup window of iso-clips, where the one corresponding to the contact of the wall with the continuous fluid handles ranges from 0.3 to 1 of the primary phase volume fractions, while the one corresponding to the contact with the secondary fluid handles ranges from 0 to 0.3.

Although the surfaces of interest have already been created, the tool that Fluent allows to configure the three-dimensional visualization is the creation of a *Mesh* equivalent to each surface

in the *Results* section. Figure C25 shows that, among other available setups, it is possible to adjust the color used in the surface display, just as defining only the *Faces* to be visible.

Figure C24

Configuration of the iso-clip surfaces

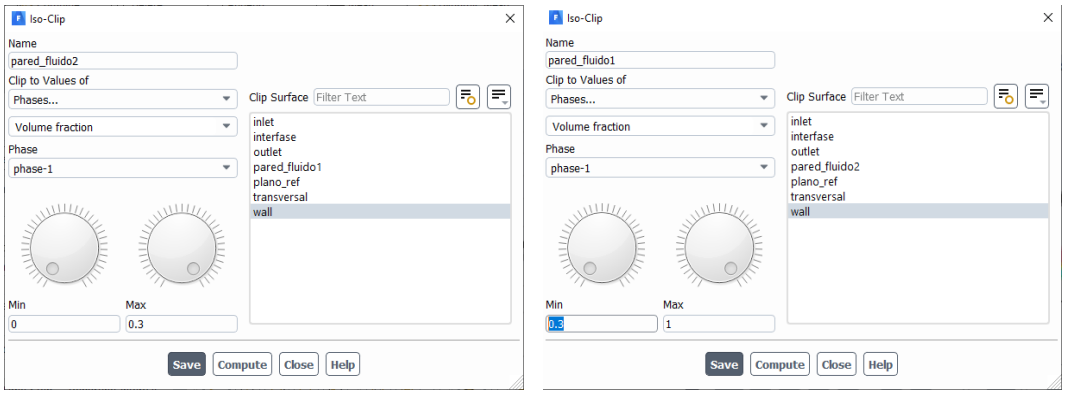

Figure C25

Mesh display configuration to personalize surfaces visualization

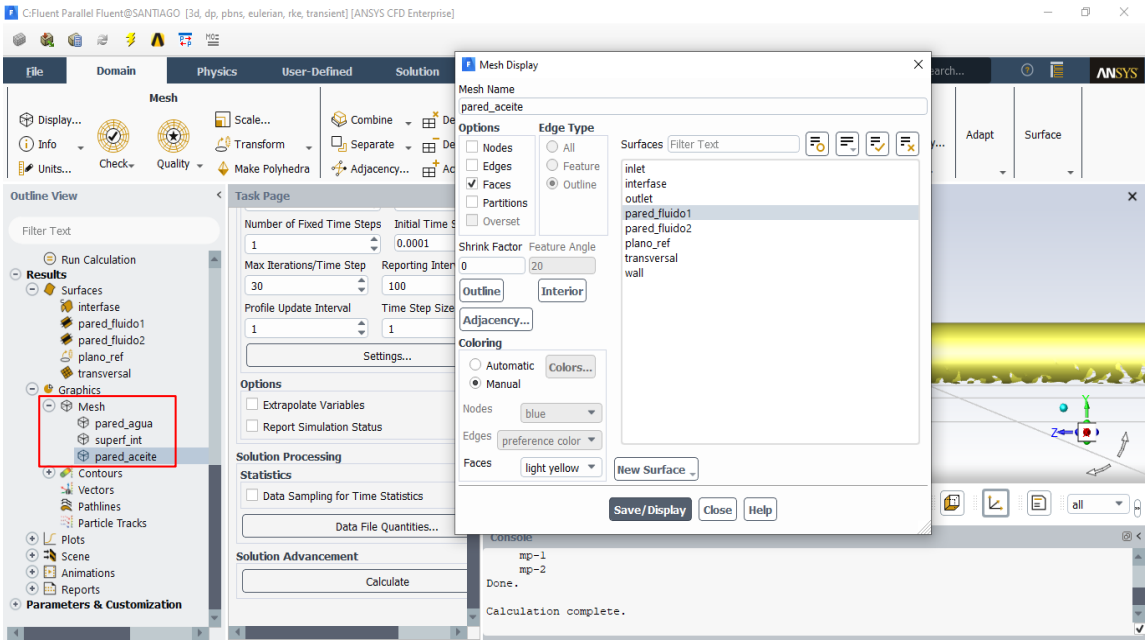

Finally, in a *Scene*, accessible in the *Results* section, the transparency of the surfaces is configured to correctly visualize the interface as seen in Figure C26.

Figure C26

Display of the Scene containing the three-dimensional pattern representation

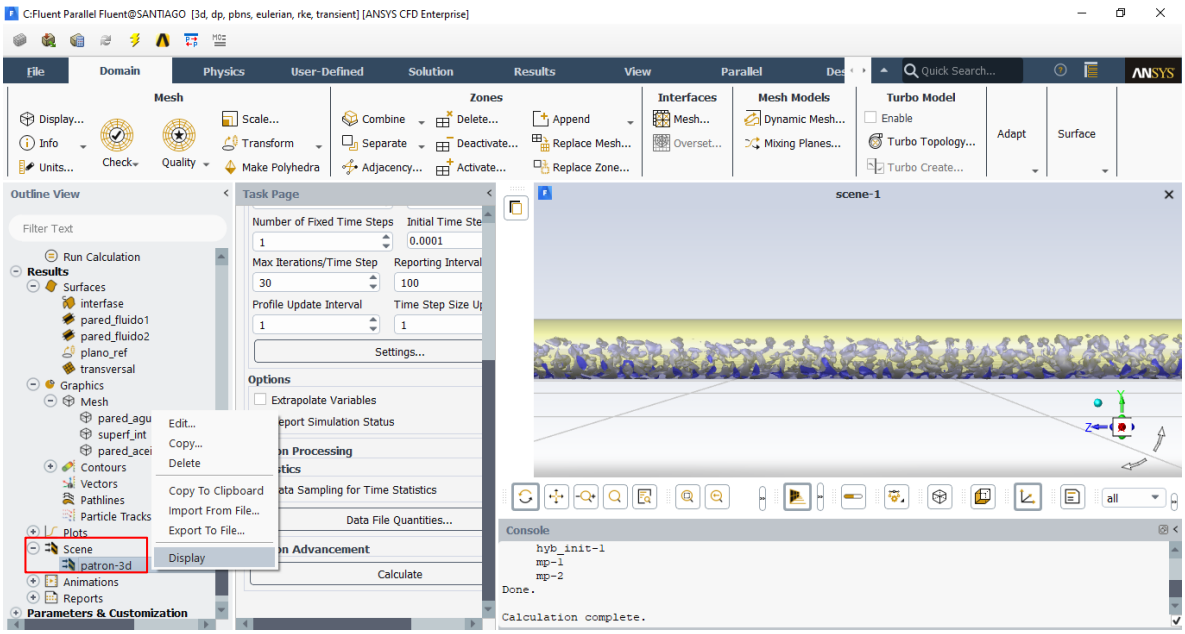

Appendix D. Tcl/Tk Code implemented in ICEM CFD

```
# Replay file ICEM CFD 2020 R1 in Workbench 2.0 Framework
# unloading mesh
ic_unload_mesh
# unloading blocking
ic_hex_unload_blocking
# delete empty parts
ic_delete_empty_parts
# reset bodies and blocks
ic_geo_reset_bodies
ic_undo_group_begin
ic_hex_delete_blocks {BLOCK_INI}
ic_undo_group_end

# rotate geometry if needed
set zref [expr {round(1000*[ic_geo_distance_from_surfaces [ic_geo_get_objects surface
      INLET] {0 0 0}])/1000.}]
mess "$zref\n"
ic_undo_group_begin
ic_undo_group_begin
if {$zref != 0} {ic_move_geometry all patterns * rotate 180 rotate_axis {0 1 0} cent
      [list 0 0 [expr {$zref/2}]] detach 0}
ic_undo_group_end
ic_geo_reset_data_structures
ic_undo_group_end

# create block
ic_undo_group_begin
ic_geo_new_family BLOCK_INI
ic_boco_set_part_color BLOCK_INI
ic_hex_initialize_blocking {} BLOCK_INI 0 101
ic_hex_unblank_blocks
ic_hex_multi_grid_level 0
ic_hex_projection_limit 0
ic_hex_default_bunching_law default 2.0
ic_hex_floating_grid off
ic_hex_transfinite_degree 1
ic_hex_unstruct_face_type one_tri
ic_hex_set_unstruct_face_method uniform_quad
ic_hex_set_n_tetra_smoothing_steps 20
ic_hex_error_messages off_minor
ic_undo_group_end

# vinculation of inlet face
set edg_in [ic_geo_get_srf_edges [ic_geo_get_objects surface INLET]]
ic_undo_group_begin
ic_hex_create_composite $edg_in
ic_hex_set_edge_projection 25 21 0 1 [lindex $edg_in 0]
ic_hex_set_edge_projection 21 37 0 1 [lindex $edg_in 0]
ic_hex_set_edge_projection 37 41 0 1 [lindex $edg_in 0]
ic_hex_set_edge_projection 41 25 0 1 [lindex $edg_in 0]
```

```
ic_undo_group_end

# vinculation of outlet face
set edg_out [ic_geo_get_srf_edges [ic_geo_get_objects surface OUTLET]]
ic_undo_group_begin
ic_hex_create_composite $edg_out
ic_hex_set_edge_projection 22 26 0 1 [lindex $edg_out 0]
ic_hex_set_edge_projection 26 42 0 1 [lindex $edg_out 0]
ic_hex_set_edge_projection 42 38 0 1 [lindex $edg_out 0]
ic_hex_set_edge_projection 38 22 0 1 [lindex $edg_out 0]
ic_undo_group_end

# projection of vertices
ic_undo_group_begin
ic_hex_project_to_surface WALL OUTLET INLET BLOCK_INI
ic_undo_group_end

# diameter calculation
set sum 0.
foreach elem [ic_geo_crv_length $edg_in] {set sum [expr {$sum + $elem}]}
set diam [expr {round(10000*$sum/3.1415926535897931)/10000.}]
mess "Diametro: $diam\n"

# o-grid block generation
ic_hex_mark_blocks unmark
ic_undo_group_begin
ic_hex_mark_blocks face_neighbors corners { 26 42 22 38 } { 25 41 21 37 }
ic_hex_ogrid 0.7 m WALL OUTLET INLET BLOCK_INI -version 50
ic_undo_group_end
ic_undo_group_begin
ic_undo_group_end
ic_hex_mark_blocks unmark

# relevant distances
set dhor [ic_hex_get_edge_param 70 78 len]
set dver [ic_hex_get_edge_param 70 66 len]
set dinc [ic_hex_get_edge_param 70 26 len]
set daxial [ic_hex_get_edge_param 25 26 len]

# defining parameters for mesh
ic_wb2_update_parameters input
set nref [ic_wb2_get_parameter user_defined Elem_Diam]
mess "Elementos de referencia: $nref\n"
set delem [expr {$diam/$nref}]
set nhor [expr {round($dhor/$delem)+1}]
set nver [expr {round($dver/$delem)+1}]
set ninc [expr {round($dinc/$delem)+3}]
set naxial [expr {(10*round(0.05*$daxial/$delem))+1}]
set xini [expr {0.6/($ninc-1)}]

# premesh parameter for horizontal edges
ic_undo_group_begin
```

```
ic_hex_set_mesh 26 42 n $nhor h1rel 0.0 h2rel 0.0 r1 2 r2 2 lmax 0 default
      copy_to_parallel unlocked
ic_undo_group_end

# premesh parameter for vertical edges
ic_undo_group_begin
ic_hex_set_mesh 26 22 n $nver h1rel 0.0 h2rel 0.0 r1 2 r2 2 lmax 0 default
      copy_to_parallel unlocked
ic_undo_group_end

# premesh parameter for inclined edges
ic_undo_group_begin
ic_hex_set_mesh 26 70 n $ninc h1rel $xini h2rel $xini r1 2 r2 2 lmax 0 geo1
      copy_to_parallel unlocked
ic_undo_group_end

# premesh parameter for axial edges
ic_undo_group_begin
ic_hex_set_mesh 26 25 n $naxial h1rel 0.0 h2rel 0.0 r1 2 r2 2 lmax 1e+10 default
      copy_to_parallel unlocked
ic_undo_group_end

# unstructured mesh creation
set folder [string range [file normalize $::auto_path] 0 [expr {[string first "\{"
      [file normalize $::auto_path]]-1}]]
set filedir ""
append filedir $folder "hex.uns"
ic_hex_create_mesh WALL OUTLET INLET BLOCK_INI proj 2 incremental dim_to_mesh 3
ic_hex_write_file $filedir WALL OUTLET INLET BLOCK_INI proj 2 dim_to_mesh 3 no_boco
ic_uns_load $filedir 3 0 {} 1
ic_uns_update_family_type visible {INLET WALL OUTLET ORFN BLOCK_INI} {!LINE_2 QUAD_4
      !HEXA_8} update 0
ic_boco_solver
ic_boco_clear_icons
```